

WALLABY Early Science - I. The NGC 7162 Galaxy Group.

T.N. Reynolds^{1,2,3*}, T. Westmeier^{1,3}, L. Staveley-Smith^{1,3}, A. Elagali^{1,2,3}, B.-Q. For^{1,3}, D. Kleiner², B.S. Koribalski^{2,3}, K. Lee-Waddell², J.P. Madrid², A. Popping^{1,4}, J. Rhee^{1,3}, M. Whiting², O.I. Wong^{1,3}, L.J.M. Davies¹, S. Driver¹, A. Robotham^{1,3}, J.R. Allison^{3,5}, G. Bekiaris², J.D. Collier^{2,7,8}, G. Heald^{3,6}, M. Meyer^{1,3}, A.P. Chippendale², A. MacLeod², M.A. Voronkov²

¹International Centre for Radio Astronomy Research (ICRAR), The University of Western Australia, 35 Stirling Hwy, Crawley, WA, 6009, Australia

²CSIRO Astronomy and Space Science, Australia Telescope National Facility, P.O. Box 76, Epping NSW 1710, Australia

³ARC Centre of Excellence for All Sky Astrophysics in 3 Dimensions (ASTRO 3D)

⁴ARC Centre of Excellence for All-sky Astrophysics (CAASTRO)

⁵Sub-Dept. of Astrophysics, Department of Physics, University of Oxford, Denys Wilkinson Building, Keble Rd., Oxford, OX1 3RH, UK

⁶CSIRO Astronomy and Space Sciences, Australia Telescope National Facility, PO Box 1130, Bentley, WA 6102, Australia

⁷School of Computing, Engineering and Mathematics, Western Sydney University, Locked Bag 1797, Penrith, NSW 2751, Australia

⁸The Inter-University Institute for Data Intensive Astronomy (IDIA), Department of Astronomy, University of Cape Town, Rondebosch, 7701, South Africa

Accepted XXX. Received YYY; in original form ZZZ

ABSTRACT

We present Widefield ASKAP L-band Legacy All-sky Blind Survey (WALLABY) early science results from the Australian Square Kilometre Array Pathfinder (ASKAP) observations of the NGC 7162 galaxy group. We use archival HIPASS and Australia Telescope Compact Array (ATCA) observations of this group to validate the new ASKAP data and the data reduction pipeline ASKAPSOFT. We detect six galaxies in the neutral hydrogen (HI) 21-cm line, expanding the NGC 7162 group membership from four to seven galaxies. Two of the new detections are also the first HI detections of the dwarf galaxies, AM 2159-434 and GALEXASC J220338.65-431128.7, for which we have measured velocities of $cz = 2558$ and $cz = 2727$ km s⁻¹, respectively. We confirm that there is extended HI emission around NGC 7162 possibly due to past interactions in the group as indicated by the 40° offset between the kinematic and morphological major axes for NGC 7162A, and its HI richness. Taking advantage of the increased resolution (factor of ~ 1.5) of the ASKAP data over archival ATCA observations, we fit a tilted ring model and use envelope tracing to determine the galaxies' rotation curves. Using these we estimate the dynamical masses and find, as expected, high dark matter fractions of $f_{\text{DM}} \sim 0.81 - 0.95$ for all group members. The ASKAP data are publicly available.

Key words: galaxies: kinematics and dynamics – galaxies: groups – galaxies: distances and redshifts – radio lines: galaxies – instrumentation: interferometers – telescopes

1 INTRODUCTION

A galaxy's environment is known to have a strong impact on its morphology. Dressler (1980) first demonstrated the morphology-density relation from optical observations,

where, with increasing galaxy density, the fraction of early-type, ellipticals increases and the fraction of late-type, spirals and irregulars decreases. The morphology-density relation indicates that over-dense environments shape the evolution of galaxies through the merger history and the accretion and stripping of neutral hydrogen gas, HI, which affects star-formation history. Radio observations of HI provide another

* tristan.reynolds@research.uwa.edu.au

window on the environmental impact in situ. H I observations show a dependence of gas content with environment as spiral galaxies in dense environments, such as towards the centre of clusters, often have less H I and reduced star formation rates compared to isolated, field galaxies of the same size and morphology (e.g. Giovanelli & Haynes 1985; Solanes et al. 2001; Dénes et al. 2014; Odekon et al. 2016). The H I mass function has also been shown to vary with galaxy environment and morphological type (e.g. Zwaan et al. 2005; Jones et al. 2018). It follows that the density of the group and cluster environments influence the physical mechanisms responsible for changing galaxy H I composition and morphology.

Ram pressure stripping (the removal of H I gas and stars from a galaxy passing through a dense intergalactic medium, Gunn & Gott 1972; Chung et al. 2009) and harassment (interacting galaxies with high relative velocities, Moore et al. 1996, 1998) are more common in clusters. In small groups, tidal stripping (low relative velocities between interacting galaxies, Moore et al. 1999; Koribalski & López-Sánchez 2009; English et al. 2010) and starvation (hot gas removed from the galaxy’s extended halo, disrupting gas accretion, cutting off further gas infall onto the galaxy and quenching of star formation, Larson et al. 1980) are more typical. Physical mechanisms more commonly seen in clusters also act in groups. For instance, ram pressure stripping has been observed even in low density groups (e.g. Rasmussen et al. 2006, 2012; Westmeier et al. 2011).

The H I content and physical mechanisms affecting galaxies in high density cluster environments have been well studied in the local Universe (e.g. Kenney et al. 2004; Jaffé et al. 2015), in part due to the ability to efficiently observe a large number of galaxies in a small area of sky. Lower density group environments have been less studied due to the significantly increased telescope time required to obtain a galaxy sample comparable to even a single cluster.

Groups are important as they are the most common environment in which to find galaxies (e.g. Tully 1987;ourgoulhon et al. 1992). The environment begins to affect the H I content and evolution of galaxies while they are in low density groups. This physical process is known as pre-processing (e.g. Wevers et al. 1984; Zabludoff & Mulchaey 1998; Kern et al. 2008; Freeland et al. 2009; Kilborn et al. 2009; Koribalski 2012; Hess & Wilcots 2013). In recent years, morphological and kinematic studies of individually resolved galaxy groups (e.g. Koribalski & Dickey 2004; Koribalski & Manthey 2005; Kilborn et al. 2005; Serra et al. 2013; Serra et al. 2015b; Hess et al. 2017) and surveys of a few dozen resolved groups (e.g. Brough et al. 2006; Kilborn et al. 2009; Pisano et al. 2011) have begun to build up a picture of H I in the group environment. However, large statistical samples currently only exist of global H I properties from surveys on single dish telescopes (e.g. HIPASS and ALFALFA, Barnes et al. 2001; Haynes et al. 2018, respectively). Complementary to group studies are deep interferometric surveys of individual galaxies, such as the Westerbork Hydrogen Accretion in Local GALaxieS survey (HALOGAS, Heald et al. 2011) and the ongoing Imaging Galaxies Inter-galactic and Nearby Environment survey (IMAGINE, PI A. Popping) and the MeerKAT Observations of Nearby Galactic Objects - Observing Southern Emitters survey (MHONGOOSE, de Blok et al. 2017) providing a comparison to the group en-

vironment. Large surveys of resolved isolated galaxies and galaxy groups require the ability to replicate the survey speed of single dish telescopes, but with increased resolution only achievable with an interferometer.

Additionally, resolved H I observations are used for estimating the total dynamical and dark matter masses of galaxies using their rotation curves (e.g. de Blok et al. 2001, 2008; Sofue & Rubin 2001; Oh et al. 2008, 2011, 2015; Westmeier et al. 2011, 2013). This is also one of the goals of the Local Volume H I Survey (Koribalski et al. 2018; Oh et al. 2018). A clear advantage of interferometric H I surveys, like WALLABY, will be the ability to map the dark matter distribution in gas-rich galaxies across the entire southern sky. If the central ~ 2 kpc are resolved, H I rotation curves can also be used to differentiate among various proposed dark matter density profiles (e.g. pseudo-isothermal and NFW, Begeman et al. 1991; Navarro et al. 1997, respectively).

1.1 ASKAP

Traditionally, radio telescopes built from paraboloidal reflector antennas have used large, single pixel feed-horn receivers, which limits the number of receivers that can be placed simultaneously at the focus of the antenna (e.g. 13 on the Parkes radio telescope multi-beam receiver). Phased array feeds (PAFs) are a recently developed type of receiver consisting of a plane of antenna elements that can form multiple beams on the sky simultaneously. The CSIRO Australian Square Kilometre Array Pathfinder (ASKAP) telescope is fitted with PAFs (DeBoer et al. 2009; Hampson et al. 2012; Hotan et al. 2014; Schinckel & Bock 2016), which consist of 188 connected dipoles in a chequerboard pattern (Hay & O’Sullivan 2008) and can form up to 36 dual-polarisation beams on the sky, simultaneously covering a significantly larger area in a single pointing than traditional receivers. PAFs are the ideal receiver to expand an interferometer’s instantaneous field of view, as antennas in an interferometric array are generally too small to accommodate multiple feed-horn receivers at the focus (i.e. 12 m vs 64 m diameter dish for ASKAP and Parkes, respectively).

The Widefield ASKAP L-band Legacy All-sky Blind Survey (WALLABY, Koribalski 2012) is one of the surveys that will take advantage of the wide field of view of the ASKAP PAFs. WALLABY will cover $\sim 75\%$ of the sky observing an estimated 500000 galaxies in H I out to $z < 0.26$ (Duffy et al. 2012). Prior to the survey commencing, several early science fields, each a single 30 deg^2 field using 12 antennas (ASKAP-12) and limited bandwidth, have been observed for testing of ASKAP and validation of the ASKAP data reduction pipeline (ASKAPSOFT). This work presents early science observations carried out with reduced bandwidths of 48, 192 and 240 MHz rather than the full ASKAP bandwidth of 304 MHz.

1.2 The NGC 7162 Galaxy Group

In this work we present the first ASKAP observations of the galaxy group consisting of NGC 7162, NGC 7162A, NGC 7166 and ESO 288-G025 (Maia et al. 1989; Fouque et al. 1992). We also detect three additional galaxies, which we identify as possible group members: ESO 288-G033,

AM2159-434 and GALEXASC J220338.65-431128.7. The galaxies cover a velocity range of $\sim 2150 - 2750 \text{ km s}^{-1}$ and are located within a $\sim 1.5 \times 1.5$ square degree area centred on $\alpha, \delta = 22:01:00, -43:30:00$; J2000. If we assume a distance to the group of $\sim 33.7 \text{ Mpc}$, NGC 7162 and NGC 7162A have a projected separation of $\sim 140 \text{ kpc}$ and the most distant group member, ESO 288-G025, has a projected separation of $\sim 332 \text{ kpc}$ from NGC 7162. We list archival and new galaxy parameters in Table 3. For computed galaxy luminosity distances, we assume velocity uncertainties of 200 km s^{-1} from peculiar velocities (e.g. Springob et al. 2014), giving distance uncertainties of $\sim 3.0 \text{ Mpc}$. The NGC 7162 group is ~ 3.8 degrees to the north-west of the NGC 7232 triplet at the centre of the WALLABY early science field. Results of NGC 7232 triplet and IC 5201, also located near the centre of the NGC 7232 field, will be presented in Lee-Waddell et al. (in prep.) and Kleiner et al. (in prep.), respectively. There are also archival observations covering NGC 7162, NGC 7162A and ESO 288-G033 taken with the Australia Telescope Compact Array (ATCA), which we use for validation of the ASKAP data.

We briefly summarise earlier radio observations of the different galaxies of the NGC 7162 group. NGC 7162 and NGC 7162A are late type spirals, detected and included in the H I Parkes All-Sky Survey catalogue (HIPASS, sources HIPASS J2159-43 and HIPASS J2200-43, respectively, Meyer et al. 2004). Note however, the HIPASS detection of NGC 7162 is confused with NGC 7162A due to the Parkes beam size ($\sim 15.5 \text{ arcmin}$), so the HIPASS measured spectrum and total flux for both galaxies are not separated. ESO 288-G025 and ESO 288-G033 are late type spirals, which are marginally detected in the HIPASS data, but not included in the HIPASS catalogue. AM2159-434 and GALEXASC J220338.65-431128.7 are dwarf galaxies with no previous H I detection or distance measurement.

This paper is structured as follows. In Section 2 we describe the ASKAP and ATCA observations and data reduction process. We present H I moment maps and spectra in Section 3 and our validation of the ASKAP observations and processing pipeline (ASKAPSOFT¹). We use tilted-ring modelling and envelope tracing to derive the rotation curves and carry out mass modelling to estimate the dark matter mass in the galaxies in Sections 4 and 5. In Section 6 we calculate the H I gas mass and deficiencies of the group spiral galaxies. We present our discussion and conclusions in Sections 7 and 8, respectively.

Throughout, we use J2000 coordinates, dates in UTC, velocities in the optical convention (cz) and the heliocentric reference frame. Galaxy quantities are calculated using distances derived from velocities converted to the local group (LG) frame², adopting a flat Λ CDM cosmology using $(H_0, \Omega_m) = (67.7, 0.307)$, concordant with the latest *Planck* results (Planck Collaboration et al. 2016).

¹ Complete documentation of the current ASKAPSOFT version can be found at <http://www.atnf.csiro.au/computing/software/askapsoft/sdp/docs/current/index.html>

² Heliocentric to local group reference frame velocity correction calculated using the NED Velocity Correction Calculator, https://ned.ipac.caltech.edu/forms/vel_correction.html

2 OBSERVATIONS AND DATA REDUCTION

2.1 ASKAP

NGC 7162A and NGC 7162 lie in the top right corner (north west) beams of the WALLABY early science field centred on the NGC 7232 galaxy group ($\sim 2.5 \times 2.5$ square degrees centred on $\alpha, \delta = 22:00:00.0, -43:30:00.0$). WALLABY early science observations are carried out with beams arranged in a 6×6 square grid resulting in a field of view of 30 square degrees. This beam arrangement is used for two footprints on the sky (A, centred on $\alpha, \delta = 22:13:07.7, -45:16:57.1$, and B, centred on $\alpha, \delta = 22:10:35.41, -44:49:50.7$), with footprint B offset by $0^\circ.64$ from footprint A. This configuration allows us to obtain uniform sensitivity across the sky, within the overlap region, by combining the two footprints. ASKAP beams are formed by pointing the antennas at the Sun prior to the start of observing using the maximum signal-to-noise ratio (maxSNR, Applebaum 1976) method (for details see Chippendale et al. 2015; McConnell et al. 2016). This early science field was observed over 14 nights in August and October of 2016 and 2 nights in August and September of 2017 for a total of 175.3 hrs with 8 nights in footprint A and 8 nights in footprint B (see Fig. 1 for the beam positions on the sky for footprint A and B, green and magenta circles, respectively). These observations used an array of 10 – 12 antennas from ASKAP-12. We use only 6 beams (2 footprint A, 4 footprint B) and a limited bandwidth of 8 MHz (432 channels) centred on the group (1409.56 MHz) to keep data volume and computing requirements manageable, in order to facilitate software testing and debugging. Table 1 summarises the observations from both ASKAP and ATCA.

2.1.1 ASKAPSOFT

We reduced the ASKAP observations using a preliminary version of ASKAPSOFT, the data reduction pipeline built for handling ASKAP data. Full details on ASKAPSOFT will be presented in Whiting et al. (in prep.) and Kleiner et al. (in prep.). We only give a brief summary here as our procedure only deviates at a couple steps from the standard pipeline. ASKAPSOFT first splits visibilities formed for individual beams from the observation. These are then flagged, have bandpass and gain calibrations applied and are imaged separately before mosaicking beam images together. Our primary calibrator is PKS 1934-638, which we use for flux and bandpass calibration. Some additional manual flagging of the first two hours from the footprint B visibilities was required on the shortest baseline to remove solar interference. After flagging and calibrating the observations, ASKAPSOFT creates a continuum sky model which is used to perform continuum subtraction on the spectral uv data (i.e. the model is used to simulate visibilities which are then subtracted from the observed visibilities).

The default ASKAPSOFT pipeline can only handle a single night's observation for imaging, limiting the depth to which we can CLEAN to three times the root-mean-square (RMS) noise level of a single night ($3\sigma \sim 18 \text{ mJy beam}^{-1}$). Image combination is then carried out in the image plane by linear mosaicking the beams from individual nights. To lower the threshold to which we can CLEAN, we used a modified pipeline script for imaging to combine data in

the uv-domain. Using this script, we can feed the imager multiple nights of uv-domain data for a single beam and footprint. We imaged using a resolution of $5'' \text{ pixel}^{-1}$ and 4 km s^{-1} channels, with `ROBUST` = 0.5 and a Gaussian taper of $30''$, resulting in a synthesised beam of $39'' \times 34''$. With the modified imaging script we imaged 8 nights worth of data, lowering the RMS and improving our deconvolution ($3\sigma \sim 9 \text{ mJy beam}^{-1}$). We do not achieve a $\sqrt{8}$ improvement in the RMS due to different integration times, percentage of flagged data and number of antennas used each night (see Section 3.3). For deconvolution, we use the multi-scale CLEAN algorithm (e.g. Cornwell 2008; Rau & Cornwell 2011) on scales of 0 (point sources), 3, 10 and 30 pixels. We set the major cycle CLEAN threshold to 3σ and for the minor cycle 4.5σ . These parameters were fine-tuned to maximize the amount of flux recovered after deconvolution. Prior to mosaicking the imaged beams, we first removed residual continuum emission, visible due to the decreased RMS level ($\sim 3 \text{ mJy beam}^{-1}$), using image-based continuum subtraction (e.g. subtracting a 2nd order polynomial fit to residual continuum flux from the data cube). Our final mosaicked cube RMS level is $\sim 2.3 \text{ mJy beam}^{-1}$. We note that full ASKAP (36 antennas) will be much more sensitive than ASKAP-12 and will reach WALLABY sensitivity ($1.6 \text{ mJy beam}^{-1}$) in a single 12 hr observation.

2.1.2 MIRIAD

In addition to performing imaging with ASKAPSOFT, we also imaged using MIRIAD (Sault et al. 1995) for validation purposes. Similar to ASKAPSOFT, we imaged all the flagged, calibrated and continuum subtracted uv-data beam by beam with the task `INVERT`, using the same pixel and spectral resolution, robustness and taper from ASKAPSOFT. We deconvolved the dirty image using the CLEAN algorithm with a cutoff flux of 5 mJy and 8000 iterations and restored the deconvolved image using `RESTOR`. We used the task `CONTSUB` to fit and subtract a 0th order polynomial to the emission free channels to remove residual continuum emission, similar to ASKAPSOFT. We finally create a mosaicked image cube using the task `LINMOS`, applying primary beam correction assuming a $1^\circ \times 1^\circ$ Gaussian and weighting each beam cube by the image RMS. The RMS of the mosaicked MIRIAD imaged data is comparable to that obtained imaging with ASKAPSOFT (~ 2.2 vs $2.3 \text{ mJy beam}^{-1}$, respectively). The synthesised beam, $37'' \times 32''$, is $\sim 2''$ smaller than the one produced using ASKAPSOFT. We note that MIRIAD is unable to image the ASKAP data perfectly as it does not account for non-coplanar baselines, which can be accounted for using the w-projection algorithm (Cornwell et al. 2008), and may cause position shifts and minor imaging artefacts.

2.2 ATCA

The archival Australia Telescope Compact Array (ATCA) observations of NGC 7162, NGC 7162A and ESO 288-G033, were obtained under project ID C2573 (Observer: S. Reeves) for a single pointing centred on NGC 7162A (Fig. 1, solid orange circle), using the 750D antenna configuration (Reeves et al. 2015) and the Compact Array Broadband Backend system (CABB, Wilson et al. 2011). The flux and phase cal-

ibrators observed were PKS 1934-638 and PKS 2106-413, respectively. The total on-source integration time was 994 min (see Table 1).

We reduced the data using MIRIAD using a standard method. After first excluding antenna 6, we interactively flagged the flux and phase calibrators and science field data using the task `BLFLAG`. We then calibrated the flux of PKS 1934-638 observations using `MFCAL`. We applied the flux calibration to the phase calibrator, PKS 2106-413, and determined time-dependent gain solutions on the phase calibrator. We then applied both phase and gain calibrations to the science observations.

We inspected the time-integrated shortest baseline (antenna 1-2) to find channels clear of any H I emission to find the continuum, which we subtracted using `UVLIN` with a 2nd order polynomial. We created a dirty map from the continuum subtracted data setting the weighting to `ROBUST` = 0.5 and a channel width of 10 km s^{-1} . We use a spectral resolution of 10 km s^{-1} instead of the raw resolution of 6.65 km s^{-1} to improve our signal to noise. We then deconvolved the dirty map using Högbom CLEAN with a 3σ cutoff flux of 6 mJy beam^{-1} and 10000 iterations before restoring the deconvolved image cube with `RESTOR`. The resulting data cube has an RMS of $1.2 \text{ mJy beam}^{-1}$, which agrees with the expected RMS for ATCA with these observation parameters ($1.1 \text{ mJy beam}^{-1}$), and a synthesised beam of $60'' \times 36''$.

3 IMAGE ANALYSIS

We use the Source Finding Application (SoFiA, Serra et al. 2015a) to locate significant H I emission in the ASKAP data cube. SoFiA provides integrated intensity (moment 0) and velocity field (moment 1) maps, integrated spectra and detected source properties, including integrated flux and line widths (w_{20} and w_{50}). In SoFiA, we set a 5σ threshold and allow the initial SoFiA source mask to expand and encompass additional voxels until the total source flux stopped increasing.

3.1 HI Maps

In our survey volume (Fig. 1) we detect six ASKAP H I sources using SoFiA, each identified with a known optical counterpart. The sources are named using the centre position defined by SoFiA (Table 2), hereafter referred to by their more common names except for GALEX-ASC J220338.65-431128.7 which we refer to as ‘J220338-431131’. We detect the original group members, NGC 7162, NGC 7162A and ESO 288-G025, while we do not detect H I in NGC 7166, in agreement with previous ATCA observations (Oosterloo et al. 2007). In addition to the group galaxy detections, we also detect H I in two nearby dwarf galaxies, AM 2159-434 ($\alpha, \delta = 22:02:50, -43:26:44$) and J220338-431131 ($\alpha, \delta = 22:03:38, -43:11:28$), with no previous H I detections and beyond the field of view of ATCA. Their projected distances from NGC 7162A, assuming a distance of 33.7 Mpc , are 300 and 328 kpc , respectively. This demonstrates the power of the wide field of view of the ASKAP for discovering previously undetected dwarf galaxies. Both dwarfs are also detected in GALEX NUV/FUV imaging indicating recent star formation. We also detect ESO 288-G033

Table 1. ATCA and ASKAP observation parameters.

Observation Parameter	ATCA	ASKAP 48 MHz	ASKAP 192 MHz	ASKAP 240 MHz
Project ID	C2573	AS035	AS035	AS035
Dates	2013 Aug 2–3	2016 Aug 11–12 2016 Oct 7–19	2017 Aug 23	2017 Sept 27
Configuration	750D	ASKAP-12	ASKAP-12	ASKAP-12
Minimum Baseline	31 m	22 – 61 m	22 – 61 m	22 – 61 m
Maximum Baseline	719 m	2300 m	2300 m	2300 m
Integration Time	994 min	160.3 hr	10 hr	5 hr
Bandwidth	64 MHz	48 MHz	192 MHz	240 MHz
Channels	2048	2592	10368	12960
Channel Width	31.25 kHz	18.5 kHz	18.5 kHz	18.5 kHz
Central Frequency	1406.0 MHz	1400.497 MHz	1344.5 MHz	1320.5 MHz
Polarisations	XX, YY	XX, YY	XX, YY	XX, YY

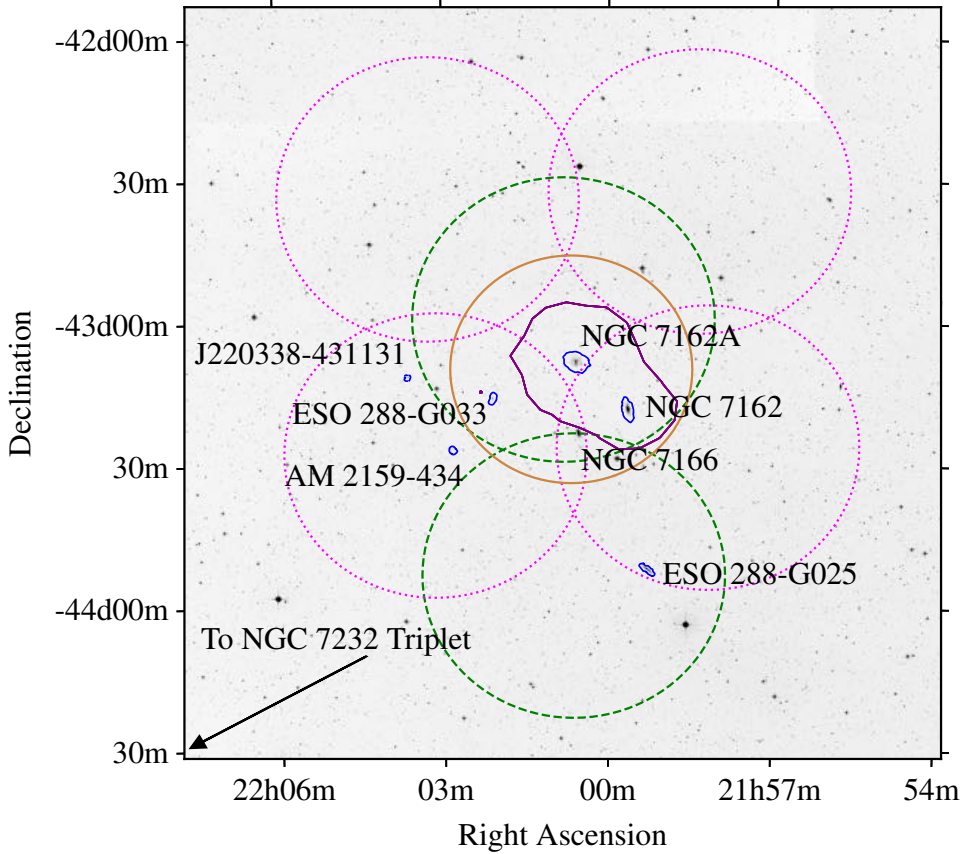


Figure 1. Digitized Sky Survey blue optical image with $1.6 \times 10^{19} \text{ cm}^{-2}$ and $2.8 \times 10^{18} \text{ cm}^{-2}$ H I column density contours overlaid from ASKAP (blue) and HIPASS (purple). The observed footprint is shown for the ASKAP footprints A (green, dashed circles) and B (magenta, dotted circles) and ATCA (orange, solid circle). The footprint A beams are numbers 16 and 35 (top and bottom, respectively). The footprint B beams are numbers 16, 35, 04, 17 (clockwise from top right). Beam numbers are from the full 36 beam footprint. The circles indicate the nominal full width at half maximum (FWHM) for each beam.

($\alpha, \delta = 22:02:06, -43:16:07$), which is within the ATCA beam of the archival observations providing an additional galaxy for validation. For the three galaxies in the ATCA beam, ATCA detects H I to larger radii than ASKAP-12 as expected for the larger ATCA synthesised beam, more compact baselines and the lower H I column density sensitivity threshold used for source finding with SoFiA ($3\sigma = 1.7 \times 10^{18} \text{ cm}^{-2}$

and $5\sigma = 9.5 \times 10^{18} \text{ cm}^{-2}$ for MIRIAD and ASKAPSOFT, respectively).

In Fig. 1, we show a Digitized Sky Survey (DSS) blue optical image of the full group with $1.6 \times 10^{19} \text{ cm}^{-2}$ H I column density contours of the detected galaxies overlaid in blue, the footprint of the ASKAP beams covering the group (green and magenta circles) and indicate the direction of

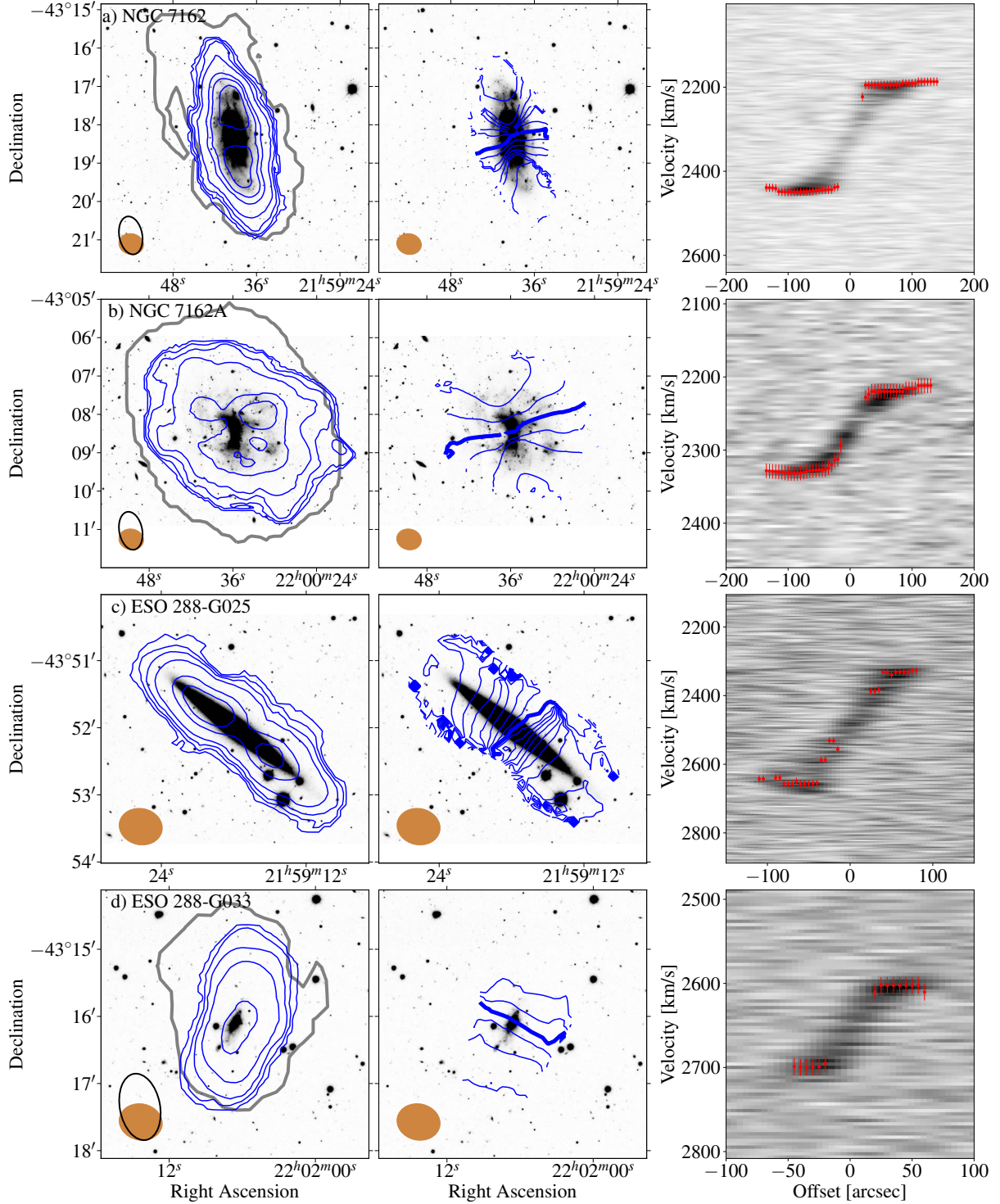


Figure 2. ASKAP H I moment maps (column density and velocity field, left hand and centre columns, respectively) of the four spiral galaxies (blue contours) overlaid onto Dark Energy Survey (DES) r -band grey scale images (Abbott et al. 2018). The panel sizes for the column density and velocity field maps are $7' \times 7'$ (a and b) and $4' \times 4'$ (c and d). Column density map contour levels are (1, 5, 10, 20, 50, 70, 100) $\times 10^{19} \text{ cm}^{-2}$. Velocity field (heliocentric reference frame) map contours levels in 20 km s^{-1} steps decreasing and increasing from the systemic velocity (thick line) of each galaxy (see Table 3). The velocity increases from the southern (lower) side (panels a and b) and increases from the northern (upper) side (panels c and d). The ASKAP synthesised beam sizes is shown in the lower left corner of the panels in the left and centre columns by the orange ellipse. We also include the 10^{19} cm^{-2} H I column density contour from ATCA (thick grey contour) for NGC 7162, NGC 7162A and ESO 288-G033, along with the ATCA synthesised beam (black ellipse). Position-Velocity diagrams (right hand column) are shown with terminal velocities measured using the envelope tracing method (red circles). We exclude points with an offset of $< \pm 20''$ from the envelope tracing.

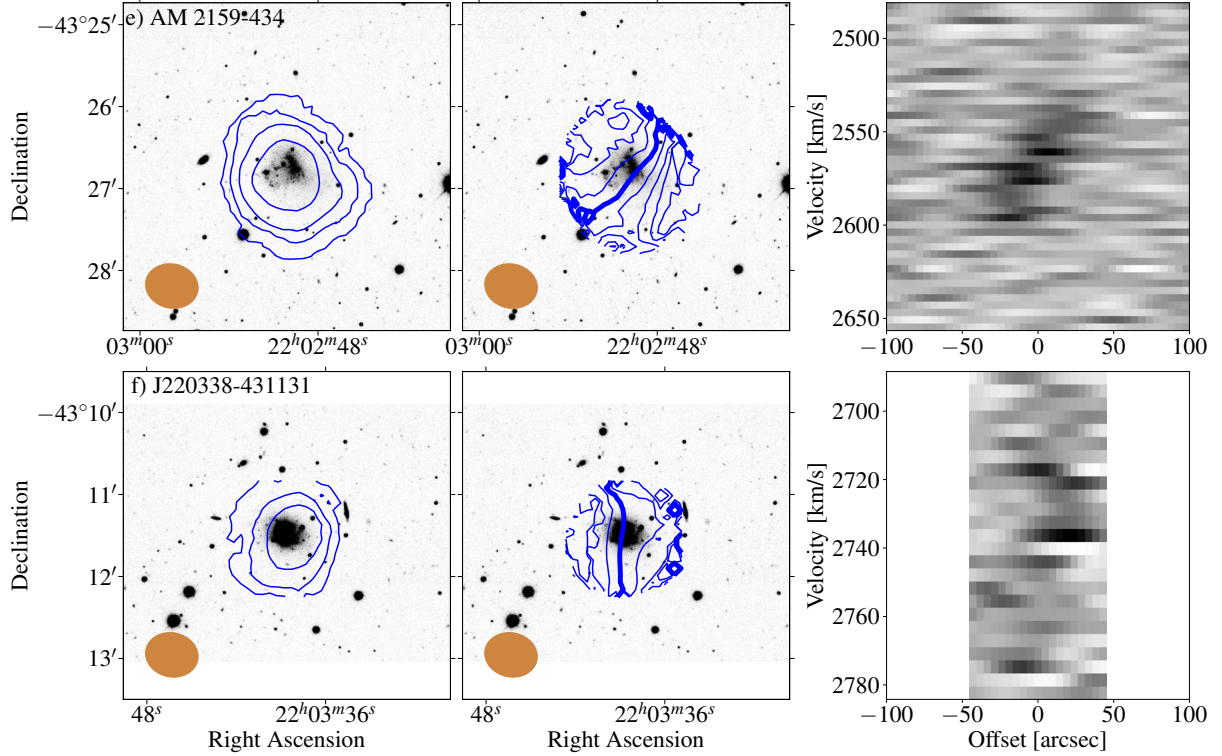


Figure 3. Similar to Fig. 2 for the two dwarf galaxies with background DES g -band grey scale images. The panel sizes for the column density and velocity field maps are $4' \times 4'$ (e and f). Column density map contour levels are $(1, 5, 10, 20, 50, 70, 100) \times 10^{19} \text{ cm}^{-2}$. Velocity field (heliocentric reference frame) map contours levels in 7 km s^{-1} steps decreasing and increasing from the systemic velocity (thick line) of each galaxy (see Table 3). The velocity increases from the western (right) side.

Table 2. WALLABY source name IDs and common galaxy names, detected in H I.

WALLABY Source ID	Galaxy
WALLABY J215939-431822	NGC 7162
WALLABY J220034-430822	NGC 7162A
WALLABY J215917-435201	ESO 288-G025
WALLABY J220206-431603	ESO 288-G033
WALLABY J220249-432652	AM 2159-434
WALLABY J220338-431131	GALEXASC J220338.65-431128.7

the NGC 7232 triplet, located at the centre of the ASKAP 36 beam footprint. We show Dark Energy Survey (DES) r - and g -band (Abbott et al. 2018) postage stamps of each H I detected spiral (r) and dwarf (g) galaxy overlaid with integrated intensity and velocity field contours and position-velocity (PV) diagrams taken along the major axis of each galaxy from SoFiA (Fig. 2 and 3: left, centre and right columns, respectively).

We use a 5σ threshold and mask dilation in SoFiA to avoid picking up sidelobe emission during source finding. We initially used a 3σ threshold for source finding to pick up any faint emission slightly above the noise level. However, this also picks up and includes sidelobe emission around our two brightest galaxies, NGC 7162 and NGC 7162A, in these galaxies' source masks. The sidelobe artefacts are due to the incomplete uv-coverage of ASKAP-12 and systematic errors in the calibration of the data. SoFiA does not pick up side-

lobes around our other four detections using the 3σ threshold as they are fainter and any sidelobes are below the image cube noise level. The CLEAN artefacts limit our ability to comment on the presence or lack of faint extended emission, as any extended emission is lost in the sidelobes using the 3σ threshold and the 5σ threshold will miss any faint emission. Even using a 5σ threshold, SoFiA still picks up the first negative sidelobe in some channels which will tend to lower the integrated fluxes. Full ASKAP will not have the same challenges as ASKAP-12 as it will have significantly improved uv-coverage with 36 antennas and a finalised pipeline using the optimal calibration and imaging parameters. Unsurprisingly, the deconvolution is not improved using MIRIAD, which has the additional w-projection issues, contributing to the flux loss in the integrated spectra (Fig. 4).

3.2 HI Spectra

One of the main objectives of early science is to compare the ASKAP data against earlier H I benchmarks such as ATCA and HIPASS observations. We compare the integrated spectra from SoFiA after processing the ASKAP observations with ASKAPSOFT and MIRIAD with ATCA (NGC 7162, NGC 7162A and ESO 288-G033) and HIPASS (NGC 7162 and NGC 7162A) observations (Fig. 4) for validation of the instrument and processing pipeline. We extract galaxy integrated spectra from the MIRIAD imaged ASKAP cube using the SoFiA source mask from the ASKAPSOFT imaged cube to ensure the spectra cover the same regions. As

mentioned in Section 2.1.2, the MIRIAD processing will introduce artefacts (e.g. distortions in source shapes and flux loss) and position errors away from the ASKAP beam centres due to MIRIAD not accounting for non-coplanar baselines. The artefacts and position errors explain the small variations we find between the spectra from the ASKAPSOFT and MIRIAD imaged data cubes (Fig. 4). The Gaussian approximation of the ASKAP beams that we use also contributes to the uncertainty in our measured fluxes as the shape of the edge beams are known to deviate from a two dimensional Gaussian (e.g. Serra et al. 2015b; Heywood et al. 2016). The combination of these uncertainties is most notable for the receding side of ESO 288-G025, closest to the beam edge, in which the spectrum from the MIRIAD cube has only recovered $\sim 66\%$ of the flux compared with the ASKAPSOFT cube between $2600 - 2700 \text{ km s}^{-1}$ (Fig. 4e).

We have good agreement between the integrated ASKAP (ASKAPSOFT, dot-dashed blue) spectra of NGC 7162 and ESO 288-G033 and those we obtain from ATCA (solid orange) observations, where the small flux loss ($\sim 6 - 10\%$) is expected due to the ATCA observations having shorter baselines than ASKAP. We have lost approximately a quarter of the flux of NGC 7162A in the ASKAP observations, with the larger flux loss due to incomplete deconvolution (Section 3.1). This has also affected NGC 7162, but only to a small extent compared to NGC 7162A. We can only compare the spectrum from the sum of the individual NGC 7162 and NGC 7162A spectra with HIPASS as the two galaxies are not fully resolved in the Parkes beam. The loss of flux in the combined spectrum relative to HIPASS (dashed red) is again due to the deconvolution process, high source finding threshold and resolving out the H I emission with ASKAP.

We can determine velocities of and distances to the two dwarf galaxies using the H I spectra. For AM 2159-434 we derive a value of $V_{\text{hel}} = 2558 \text{ km s}^{-1}$ (corresponding to $V_{\text{LG}} = 2552 \text{ km s}^{-1}$ and a luminosity distance of $D_{\text{lum}} = 37.9 \pm 3.0 \text{ Mpc}$). Similarly for J220338-431131 we derive $V_{\text{hel}} = 2727 \text{ km s}^{-1}$ (corresponding to $V_{\text{LG}} = 2722 \text{ km s}^{-1}$ and $D_{\text{lum}} = 40.5 \pm 3.0 \text{ Mpc}$).

3.3 Validation

We have used the ASKAP observations processed with ASKAPSOFT for instrument and pipeline verification. We demonstrate that the RMS noise, σ , in the final ASKAP image data cube decreases as expected assuming Gaussian noise ($\sigma \propto 1/\sqrt{\tau}$, where τ is the effective integration time in hours from multiple nights determined as the product of the integration time, number of antennas squared and percentage of unflagged data for each night of observation). We measure the RMS for footprints A and B separately as the RMS does not scale in the same manner when mosaicking footprints, as the mosaicking process applies primary beam correction (Fig. 5). The RMS in footprint A is measured in the centre of beam 16, one of the edge corner beams, and in footprint B the RMS is measured in the centre of beam 4, a corner beam of the square of beams between the central four beams and edge beams. The sensitivity of the ASKAP PAFs is known to vary as a function of beam position, with the highest sensitivity in the central four beams and the noise

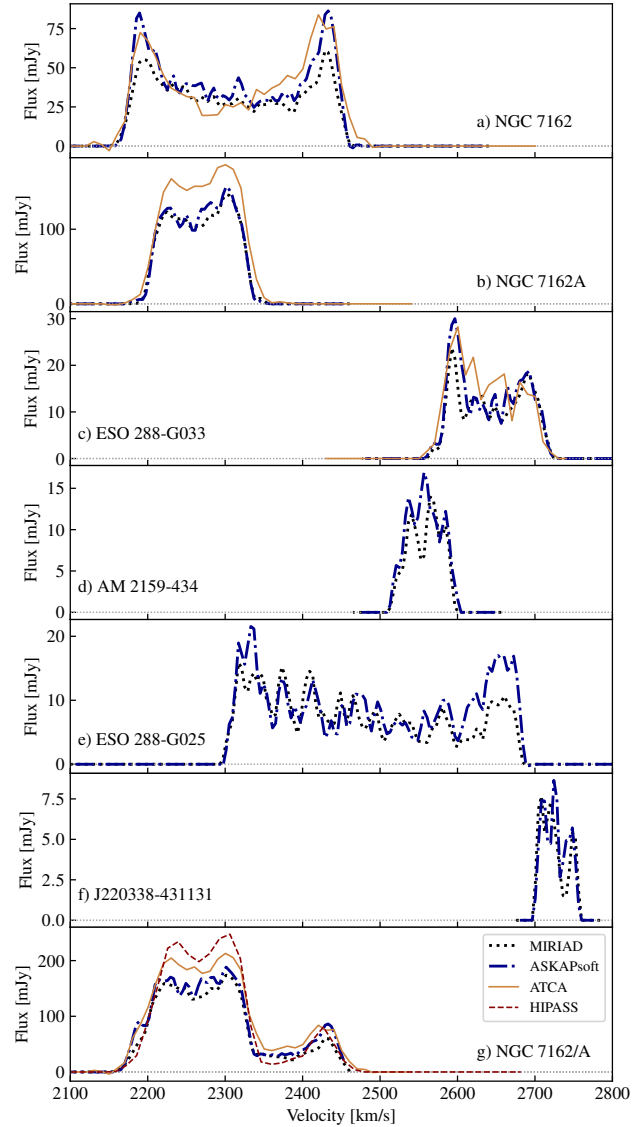


Figure 4. Panels a–f: ASKAP integrated H I spectra of our detections as obtained from SoFiA after imaging in both ASKAPSOFT (thick dot-dashed blue) or MIRIAD (thick dotted black). For comparison we also show ATCA integrated H I spectra (thin solid orange). Panel g: The combined ASKAP integrated H I spectrum of NGC 7162 and NGC 7162A (thick dot-dashed blue) with ATCA (thin solid orange) and HIPASS (thin dashed red) for comparison. We summed the ASKAP/ATCA spectra for NGC 7162 and NGC 7162A because these galaxies are not fully separated in the Parkes beam.

increasing towards the edge beams, which we see in the lower RMS in beam 4 vs 16.

For NGC 7162, NGC 7162A and ESO 288-G033, we compare the parameter output from SoFiA for the ASKAP and ATCA observations (see Table 3). The integrated fluxes and calculated H I mass for NGC 7162 and NGC 7162A from ASKAP are lower than from ATCA, which is primarily due to flux remaining in residual sidelobes and lack of short baselines. ESO 288-G033 has reasonable agreement between ASKAP and ATCA with the higher ATCA values primar-

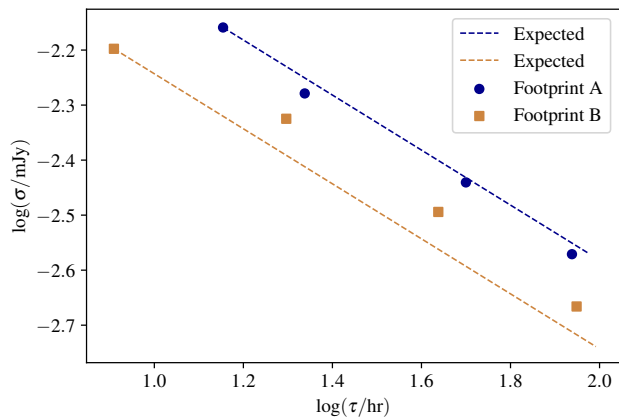


Figure 5. Image RMS noise level as a function of effective integration time τ for footprint A (blue circle) and footprint B (orange square). The expected RMS (dashed lines) are based on the data. The RMS decreases following the expected relation assuming Gaussian noise ($\sigma \propto 1/\sqrt{\tau}$, where τ is the effective integration time in hours from multiple nights determined as the product of the integration time, number of antennas squared and percentage of unflagged data for each night of observation). We only show the effective integration time for 8 nights as this the maximum we have in each footprint and the noise reduction does not scale in the same manner when combining footprints due to primary beam correction.

ily due to the shorter baselines in the ATCA configuration providing better sensitivity to diffuse emission. We find very good agreement in w_{20} and w_{50} line profile widths between both observations. We also attempt to compare the ASKAP and ATCA integrated fluxes for NGC 7162 and NGC 7162A with their HIPASS values by decomposing the HIPASS moment 0 map into two point sources using the MIRIAD task IMFIT. The uncertainties in the HIPASS integrated fluxes are only the fitting uncertainties and do not include systematic uncertainties from HIPASS, hence the true uncertainties will be larger. The HIPASS integrated flux for NGC 7162 is lower, though within errors of the ASKAP and ATCA values, indicating some of its flux has been attributed to NGC 7162A as we would expect HIPASS to recover more flux (see Table 3). HIPASS recovers more flux in NGC 7162A than either ASKAP or ATCA indicating that there is likely to be $\sim 40\%$ more diffuse H I emission in NGC 7162A, which is resolved out by the interferometers.

4 ROTATION CURVES

The advantage of ASKAP observations is the increased resolution (spatial and spectral) and sky coverage compared with archival ATCA and HIPASS data ($39'' \times 34''$, $60'' \times 36''$ and $15.5' \times 15.5'$, respectively). We can use this to determine the rotation curves for the NGC 7162 group galaxies. Using rotation curves, we can determine the galaxies' dynamical masses and dark matter content through mass modelling. Due to the different inclinations of the group galaxies (i.e. nearly face-on vs edge-on), we use two methods for determining the rotation curves: *i*) tilted ring fitting to the velocity field (e.g. Rogstad et al. 1974, Section 4.1) and *ii*)

envelope tracing of the position-velocity diagram along the galaxy's major axis (e.g. Sancisi & Allen 1979; Westmeier et al. 2013, Section 4.2). The tilted ring modelling method gives more accurate results by allowing for variations in inclination and position angle of the galaxy, but cannot be used for galaxies that are edge-on or are not sufficiently resolved (i.e. ESO 288-G025, ESO 288-G033, AM 2159-434 and J220338-431131). Hence we only use this method for NGC 7162 and NGC 7162A. We use the envelope tracing method on all galaxies and in the case of NGC 7162 and NGC 7162A we compare the results from the two techniques.

4.1 Tilted Ring Model

The tilted ring model works by fitting a series of circular isovelocity rings to the velocity field and assuming that gas particles move with a constant speed on circular orbits. We follow the method of Westmeier et al. (2011) where we use the GIPSY (van der Hulst et al. 1992; Vogelaar & Terlouw 2001) task ROTCUR and allow the inclination, i , position angle, θ , systemic velocity, v_{sys} , and centre position, (x, y) , of the rings to vary to best match the galaxy. We use 10 rings, with radius = 15 arcsec, centred on the galaxy, which is around half the ASKAP synthesised beam (this results in some correlation between adjacent points, but improves sampling of the galaxies).

We fit a tilted ring model to both sides of the galaxy together in three iterations. We first leave all parameters free (except the expansion velocity, $v_{\text{exp}} = 0 \text{ km s}^{-1}$) and take our initial guess for the galaxy centre from NED. In the second iteration we leave the position angle, inclination angle and rotational velocity free. For the third iteration, we obtain the final rotation curve by leaving only the rotational velocity free. The error in the fitted velocity field is calculated by ROTCUR using the standard deviation around the mean rotation in each ring. In Fig. 6, we show the Gauss-Hermite polynomial fit to the observed velocity field (left column), the model (centre column) and the residual (right column) velocity field for NGC 7162 and NGC 7162A (top and bottom rows, respectively). The tilted ring fit provides a good model to the data with small residuals mostly in the range -10 to 10 km s^{-1} . We also fit the tilted ring model to the approaching and receding sides of the galaxy separately to look for variations in the rotation curve and to estimate the errors in the rotational velocity, position angle and inclination angle (left and right columns of Fig. 7 for NGC 7162 and NGC 7162A, respectively). When fitting each side of each galaxy separately we keep v_{sys} and (x, y) fixed to the values derived from the fit to the full galaxy.

Both NGC 7162 and NGC 7162A have approximately constant position angles across the entire galaxy disk, so neither galaxy has a distinguishable inner and outer disk. The presence of an inner and outer disk could indicate a past interaction event (e.g. Westmeier et al. 2011, 2013). The inclination of NGC 7162 decreases towards the edge of the galaxy, while for NGC 7162A the inclination remains constant. Our tilted ring fits are unaffected by residual sidelobes, as they are below the 5σ threshold and are beyond the main disks of NGC 7162 and NGC 7162A.

There is a degeneracy between the inclination angle, i , and rotational velocity, V_{rot} , best seen for the receding side of NGC 7162A at large radii ($> 75''$) in Fig. 7d and f,

Table 3. NGC 7162 galaxy group member parameters. $V_{\text{hel}} = cz$ - velocity in the heliocentric reference frame, V_{LG} - velocity in the Local Group reference frame, respectively, i - inclination, B_{25} - 25 mag arcsec $^{-2}$ B -band, PA_{B25} , D_{25} - position angle and diameter in 25 mag arcsec $^{-2}$ B -band, respectively, D_{lum} - luminosity distance, $\log(L_X)$ - ROSAT X-ray luminosity, A_{sym} - asymmetry parameter from *Spitzer* IRAC images, M_* - stellar mass from VISTA Hemisphere Survey, SFR - average star formation rate derived from WISE 12 and 22 μm bands, sSFR - specific star formation rate, M_{Dyn} - dynamical mass, $M_{\text{HI,exp}}$ - expected H I mass for morphological type, S_{int} - integrated flux, $M_{\text{HI,obs}}$ - observed H I mass, w_{20} and w_{50} - observed integrated spectra velocity widths at 20% and 50% of the maximum intensity, PA_{kin} - kinematic position angle, DEF_{HI} - H I deficiency, M_{HI}/M_* - H I to stellar mass ratio. References: (1) [Springob et al. \(2014\)](#), (2) [de Vaucouleurs et al. \(1991\)](#), (3) [Lauberts & Valentijn \(1989\)](#), (4) [Beuing et al. \(1999\)](#), (5) [Holwerda et al. \(2014\)](#), (6) [Cluver et al. \(2017\)](#), (7) This work. Note: The stellar masses for NGC 7162 and NGC 7162A are calculated within $< 90''$ and $< 105''$, respectively, not the total stellar mass. The stellar masses for NGC 7166, ESO 288-G025 and ESO 288-G033 are total stellar mass.

	NGC 7162	NGC 7162A	NGC 7166	ESO 288-G025	ESO 288-G033	AM 2159-434	J220338-431131	ref
α (J2000)	21:59:39.1	22:00:35.7	22:00:32.9	21:59:17.9	22:02:06.64	22:02:50.06	22:03:38.62	(1)
δ (J2000)	-43:18:21	-43:08:30	-43:23:23	-43:52:01	-43:16:07.0	-43:26:44.2	-43:11:28.4	(1)
Type	SA(s)c	SAB(s)m	SA0	Scd	Sc	dwarf	dwarf	(2)
V_{hel} [km s $^{-1}$]	2314	2271	2466	2481	2641	2558	2727	(7)
V_{LG} [km s $^{-1}$]	2309	2267	2460	2473	2636	2552	2722	(7)
i [deg]	67.7	39.6	62.0	81.4	72.5	—	—	(3)
PA_{B25} [deg]	10	70	15	53	152	—	—	(3)
B_{25} [mag]	13.44	13.79	12.87	14.01	16.66	—	—	(3)
D_{25} [kpc]	27.65	23.61	—	27.39	9.83	—	—	(3)
D_{lum} [Mpc]	34.3 ± 3.0	33.7 ± 3.0	33.3 ± 3.0	36.7 ± 3.0	39.2 ± 3.0	37.9 ± 3.0	40.5 ± 3.0	(7)
$\log(L_X/\text{erg s}^{-1})$	—	—	< 40.65	—	—	—	—	(4)
Asym (3.6 μm)	0.74	0.42	—	—	—	—	—	(5)
Asym (4.5 μm)	0.51	0.54	—	—	—	—	—	(5)
$\log(M_*/M_{\odot})$	9.7 ± 0.1	9.3 ± 0.1	10.3 ± 0.1	10.0 ± 0.1	8.3 ± 0.1	—	—	(7)
SFR [$M_{\odot} \text{ yr}^{-1}$]	0.727	0.343	—	—	—	—	—	(6)
$\log(\text{sSFR}/\text{yr})$	-9.8	-9.8	—	—	—	—	—	(7)
$\log(M_{\text{Dyn}}/M_{\odot})$	11.2 ± 0.1	10.6 ± 0.1	—	10.9 ± 0.1	9.7 ± 0.2	—	—	(7)
$\log(M_{\text{HI,exp}}/M_{\odot})$	8.8 ± 0.1	8.8 ± 0.1	—	8.7 ± 0.1	8.2 ± 0.1	—	—	(7)
ASKAP								
S_{int} [Jy km s $^{-1}$]	12.37 ± 1.24	15.52 ± 1.55	—	3.66 ± 0.37	2.04 ± 0.20	0.86 ± 0.09	0.27 ± 0.03	(7)
$\log(M_{\text{HI,obs}}/M_{\odot})$	9.5 ± 0.1	9.6 ± 0.1	—	9.1 ± 0.1	8.9 ± 0.1	8.5 ± 0.1	8.0 ± 0.1	(7)
w_{20} [km s $^{-1}$]	283 ± 4	131 ± 4	—	380 ± 4	130 ± 4	81 ± 4	48 ± 4	(7)
w_{50} [km s $^{-1}$]	269 ± 4	119 ± 4	—	362 ± 4	109 ± 4	60 ± 4	45 ± 4	(7)
PA_{kin} [deg]	14	28	—	52	162	15	140	(7)
DEF_{HI}	-0.70	-0.82	—	-0.39	-0.66	—	—	(7)
$\log(M_{\text{HI}}/M_*)$	-0.2	0.3	—	-0.9	0.6	—	—	(7)
ATCA								
S_{int} [Jy km s $^{-1}$]	13.20 ± 1.32	21.02 ± 2.10	—	—	2.28 ± 0.23	—	—	(7)
$\log(M_{\text{HI,obs}}/M_{\odot})$	9.6 ± 0.1	9.7 ± 0.1	—	—	8.9 ± 0.1	—	—	(7)
w_{20} [km s $^{-1}$]	291 ± 10	142 ± 10	—	—	136 ± 10	—	—	(7)
w_{50} [km s $^{-1}$]	272 ± 10	119 ± 10	—	—	106 ± 10	—	—	(7)
DEF_{HI}	-0.72	-0.95	—	—	-0.70	—	—	(7)
HIPASS								
S_{int} [Jy km s $^{-1}$]	11.46 ± 2.58	23.06 ± 2.55	—	—	—	—	—	(7)

where V_{rot} rises sharply corresponding to a large decrease in i . This degeneracy can explain the differences at large radii between the rotation curves derived from the tilted ring and envelope tracing methods (Fig. 8). For NGC 7162, the higher V_{rot} derived from the tilted ring fit is due to the lower i compared with the constant value used for envelope tracing. We left i free in the tilted ring modelling to look for the presence of warps, which we do not find.

We determine the dynamical masses for NGC 7162 and

NGC 7162A using the rotational velocity determined from the tilted ring fit to the entire galaxy at the last radius before the fitted velocity begins rising sharply between rings (i.e. 130 km s^{-1} to 180 km s^{-1} at a radius of 135 arcsec for NGC 7162A). We find dynamical masses of $\log(M_{\text{dyn}}/M_{\odot}) = 11.2 \pm 0.1$ ($< 22.5 \text{ kpc}$) and $\log(M_{\text{dyn}}/M_{\odot}) = 10.6 \pm 0.1$ ($< 17.2 \text{ kpc}$) for NGC 7162 and NGC 7162A, respectively.

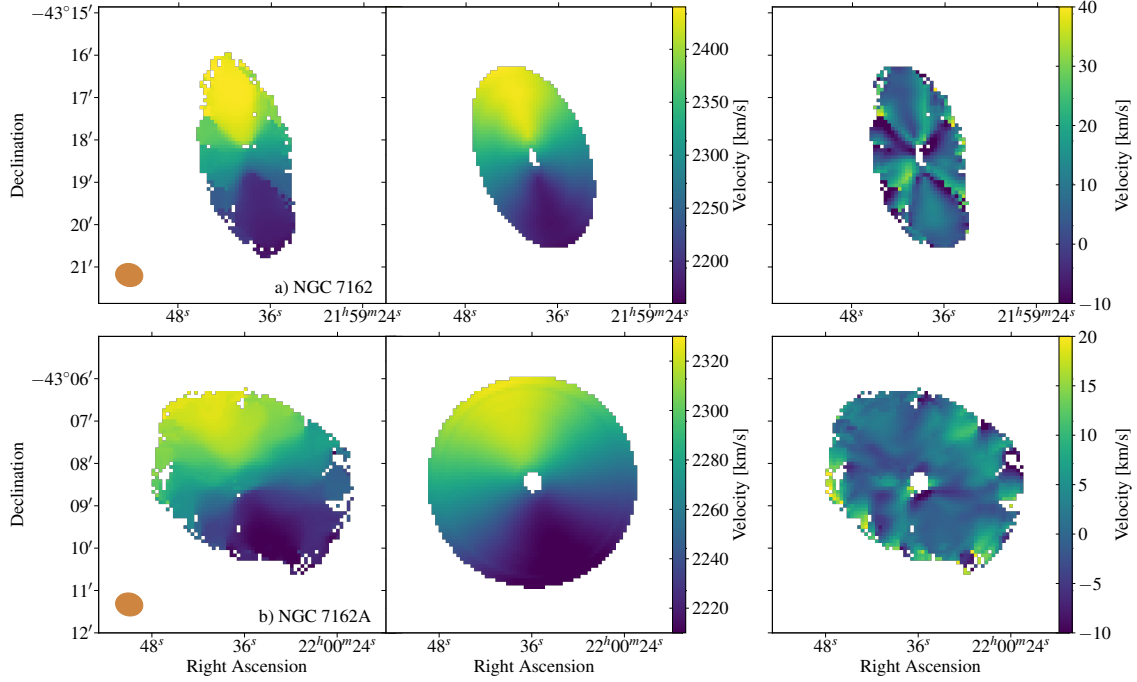


Figure 6. Gauss-Hermite polynomial fit to the observed velocity field, model and residual velocity fields (left, centre and right columns, respectively) for NGC 7162 and NGC 7162A (top and bottom rows, respectively). The observed and model velocity fields share the same colour scale. The ASKAP synthesised beam is shown by the orange ellipse in the lower left corner of the left column. The hole in the centre of the model is due to not resolving the central region with the rings with radius of $15''$.

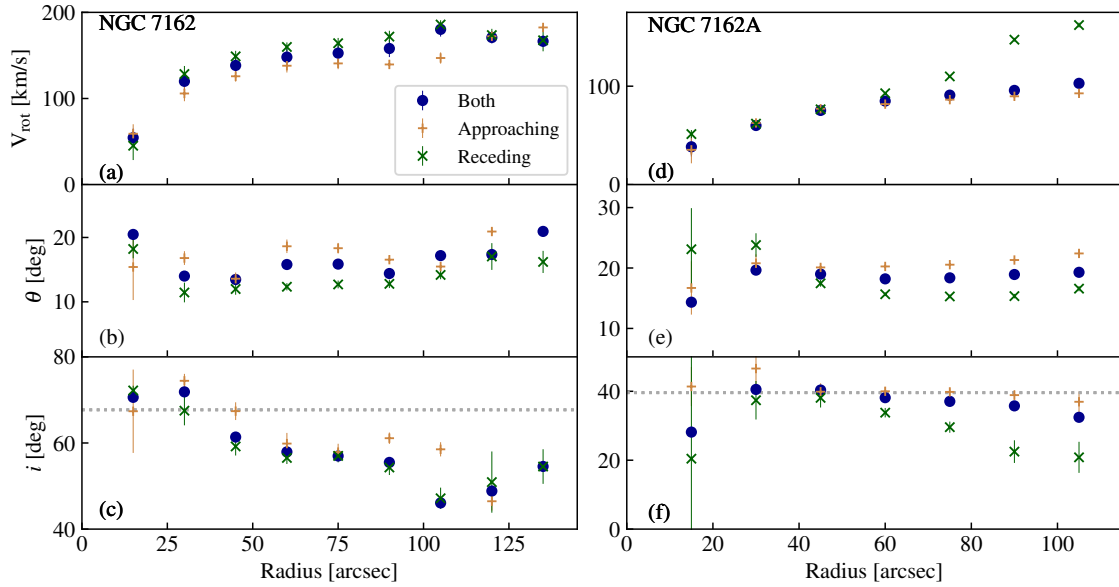


Figure 7. Rotation curve (V_{rot}), position angle (θ) and inclination angle (i) derived from tilted ring modelling of NGC 7162 and NGC 7162A (left and right columns, respectively) for both (blue circle), approaching (orange cross) and receding (green ‘x’) sides. The dashed line in panels c and f indicate the inclination angle from 25^{th} magnitude B -band optical imaging.

4.2 Envelope Tracing

The envelope tracing method derives a galaxy’s rotational velocity by finding the terminal velocity, v_t , on the edge of the galaxy facing away from the galaxy’s systemic velocity at each position taken along the galaxy’s major axis. We follow the method of Sofue & Rubin (2001); Westmeier et al. (2013)

for envelope tracing and use position-velocity (PV) diagrams along the kinematic major axis from the SoFiA output (see Fig. 2 and 3, right hand column, rotational velocities derived from envelope tracing are overlaid in red). We assume that the gas is optically thin when determining the terminal velocity of the gas. This may not be the case in the inner

regions and we exclude positions within $\pm 20''$ of the galaxy centre in our analysis. We calculate the rotational velocities using equations 1 and 2 from [Westmeier et al. \(2013\)](#). For consistency, we use a fixed inclination angle for each galaxy from the optical disk (Table 3) for deprojecting the derived rotational velocities.

We derived rotation curves for the four group spirals using the envelope tracing method. We are unable to derive a rotation curve for AM 2159-434 or J220338-431131 as we do not have inclination angles, i , for either galaxy. Additionally, the PV diagrams for AM 2159-434 and J220338-431131 are dominated by noise (Fig. 3, right column, rows e and f, respectively). We show our derived rotation curves for the approaching (blue squares) and receding (orange diamonds) sides of each galaxy in Fig. 8 and show the velocities plotted in red over the PV diagrams in the right hand column of Fig. 2. For NGC 7162 and NGC 7162A we also plot the rotation curve from the tilted ring model fitting to both sides of the galaxy (black circles). We find good agreement between the two methods for NGC 7162 and NGC 7162A. For NGC 7162A, we are able to recover the increase in rotational velocity at radii $\leq 40''$ found with the tilted ring analysis using the envelope tracing method, while for NGC 7162 the envelope tracing method is only able to recover the maximum rotational velocity. The approaching and receding sides of ESO 288-G025 are in good agreement at radii $> 40''$. ESO 288-G033, the smallest galaxy in angular size for which we could determine the rotational velocity, also has good agreement at all traced radii.

We determine the dynamical masses for ESO 288-G025 and ESO 288-G033 by taking the average of the velocity of the approaching and receding sides of each galaxy at the largest radius at which both are measured (i.e. $80''$ and $45''$, respectively). We find dynamical masses of $\log(M_{\text{dyn}}/M_{\odot}) = 10.9 \pm 0.1$ (< 14.2 kpc) and $\log(M_{\text{dyn}}/M_{\odot}) = 9.7 \pm 0.2$ (< 9.5 kpc) for ESO 288-G025 and ESO 288-G033, respectively.

5 MASS MODELLING

Using the tilted ring derived rotation curves, we model the contributions of the gaseous, stellar and dark matter components to the observed rotation curves of NGC 7162 and NGC 7162A, given by

$$v_{\text{rot}}^2(r) = f_{\text{gas}} v_{\text{gas}}^2(r) + f_{\star} v_{\star}^2(r) + v_{\text{dm}}^2(r), \quad (1)$$

where f_{gas} and f_{\star} are mass scaling factors for the gaseous and stellar disks, respectively. We use the GIPSY task ROTMAS to fit to the velocity curve for the three components given in equation (1), with the gaseous and stellar disk velocities determined from their respective mass surface densities. The mass surface density, $\Sigma(r)$, for each component is used to determine its velocity contribution to the rotational velocity. Our observations have insufficient resolution of the inner disk region to differentiate among various dark matter density profiles (e.g. pseudo-isothermal, NFW). However, we do provide estimates of the dark matter mass required for the observed rotation curve.

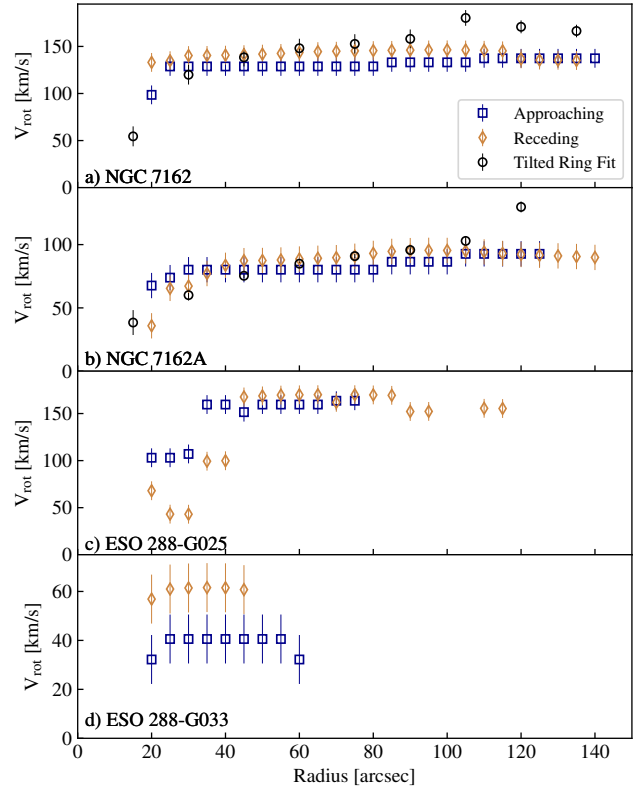


Figure 8. Rotation curves for the approaching (blue squares) and receding (orange diamonds) sides determined from envelope tracing of PV diagrams along the galaxies’ kinematic major axis from SoFiA. For NGC 7162 and NGC 7162A we plot the rotation curve from the tilted ring model fitting to both sides of the galaxy (black circles), showing good agreement.

5.1 Gas Component

The gas surface density is derived using the H I column density profile, $N_{\text{HI}}(r)$, corrected for inclination, i , taken from the tilted ring fit with

$$\Sigma_{\text{gas}}(r) = f m_{\text{H}} N_{\text{HI}}(r) \cos(i), \quad (2)$$

where the hydrogen atom mass is $m_{\text{H}} = 1.674 \times 10^{-27}$ kg and f is a correction factor accounting for the contribution of helium in the disk (we assume $f = 1.4$ for the contribution of helium, e.g. [Westmeier et al. 2011](#)). We use the GIPSY task ELLINT to calculate the H I surface density profile, which we scale by f , from the H I column density map, the total H I gas mass and the luminosity distance of the galaxy. We assume the H I gas is optically thin and is in an infinitely thin disk. The gas surface density will be underestimated if dense locations in the disk are not optically thin. The mass contribution of molecular and ionised gas can be accounted for using the scaling factor f_{gas} in equation 1.

We also scaled the total gas mass of NGC 7162A by a factor of 1.25 (i.e. to the mass from ATCA) to approximately account for the flux/mass loss due to incomplete deconvolution of the ASKAP data (~ 5.5 Jy km s $^{-1}$, Fig. 4b). We scaled to the ATCA flux rather than HIPASS due to the confusion in the HIPASS detection of NGC 7162 and NGC 7162A. However, ATCA appears to have recovered the majority

of the flux from comparison of the combined spectra of NGC 7162 and NGC 7162A from ATCA with the HIPASS spectrum (Fig. 4g). We did not apply this correction to NGC 7162 as it only suffers a small flux loss ($\sim 1 \text{ Jy km s}^{-1}$, Fig. 4a). The incomplete deconvolution most strongly affects the recovered flux of NGC 7162A as it is the brightest source with more flux left in sidelobes detectable above the noise. In Fig. 9, we show the H I mass surface density with blue squares for NGC 7162 and NGC 7162A.

5.2 Stellar Component

The stellar surface density is determined by converting the optical or near-infrared flux density, $S_\lambda(r)$, to stellar mass surface density, $\Sigma_{\text{stellar}}(r)$, using the stellar mass-to-light ratio, Υ_λ . Both the flux density and mass-to-light ratio are wavelength dependent and are determined for a specific photometric band (e.g. IRAC 3.6 and 4.5 μm bands, Westmeier et al. 2011). The mass-to-light ratio conversion uses solar units and takes the form

$$\Sigma_{\text{stellar}}(r) \sim \Upsilon_\lambda S_\lambda(r). \quad (3)$$

We use the VISTA Hemisphere Survey (VHS, McMahon et al. 2013) J - and K -band images for deriving stellar masses and surface densities. We determine stellar masses for VHS J - and K -band images using masses estimated from the Galaxy and Mass Assembly Survey (GAMA, Driver et al. 2011) and VISTA Kilo-Degree Infrared Galaxy Survey (VIKINGs) absolute magnitudes (Wright et al. 2016) for ~ 90000 galaxies. The stellar masses determined from the GAMA survey are tightly correlated (scatter of 0.1 dex) with the J - and K -band absolute magnitudes, with the relations given by

$$\log_{10}(M_*/M_\odot) = -0.454(J_{\text{abs}}) + 0.384 \quad (4)$$

and

$$\log_{10}(M_*/M_\odot) = -0.407(K_{\text{abs}}) + 1.32, \quad (5)$$

where J_{abs} and K_{abs} are the absolute magnitude in the J - and K -bands, respectively. We can then use equations 4 and 5 and the conversion from VHS image flux units, A , to magnitudes ($\text{mag} = 30 - 2.5 \log(A)$, 30 is the zero point magnitude) to derive linear relationships between stellar mass and the J - and K -band image flux units

$$M_* = 0.013 D_{\text{lum}}^{2.27} A_J^{1.135} M_\odot \quad (6)$$

and

$$M_* = 0.207 D_{\text{lum}}^{2.04} A_K^{1.02} M_\odot, \quad (7)$$

where D_{lum} is the luminosity distance. We then calculate the stellar mass from the J - and K -band images by summing the image flux in rings with the position angle and inclination of each ring determined from the tilted ring modelling for NGC 7162 and NGC 7162A (for consistency with our H I rings) and using a fixed position angle and inclination, from SoFia and optical imaging, respectively, for ESO 288-G025 and ESO 288-G033. For NGC 7162 and NGC 7162A, we calculate the stellar mass contained within a given radius ($< 90''$ and $< 105''$, respectively), corresponding to the maximum radius at which we determine the stellar surface densities (i.e. where the surface density levels off at $< 0.1 M_\odot \text{ pc}^{-2}$). We again use the GIPSY task ELLINT,

this time to derive both the stellar masses for NGC 7162, NGC 7162A, ESO 288-G025 and ESO 288-G033 and the stellar surface density profiles for NGC 7162 and NGC 7162A. We do not calculate a stellar mass for the dwarf galaxies due to foreground stars in the VHS images. Our final quoted stellar masses in Table 3 are the average of the masses found in the J - and K -bands, similarly for the stellar surface density profiles of NGC 7162 and NGC 7162A (Fig. 9). Differences in the surface density profiles derived in each band are smaller than the uncertainties. We note there are a number of factors creating uncertainty in the calculated masses including the level of dust extinction, the galaxy's initial mass function (Chabrier 2003, IMF used for GAMA), star formation history and metallicity, in addition to radial variation of these parameters within the disk (Oh et al. 2008; Westmeier et al. 2011). See Taylor et al. (2011) for details on derivation process and assumptions used in deriving GAMA masses.

We note that total stellar masses of $\log(M/M_\odot) = 10.194$ and 9.812 for NGC 7162 and NGC 7162A, respectively, were calculated from the S⁴G survey on *Spitzer* (Muñoz-Mateos et al. 2015). The *Spitzer* derived stellar masses are higher than the VHS values due to our radial cutoffs in measured values and the different IMFs assumed, Salpeter (1955) and Chabrier (2003), respectively. We can convert the stellar masses between IMFs using equation 12 from Longhetti & Saracco (2009),

$$M_{\text{Chabrier}} = 0.55 \times M_{\text{Salpeter}} \quad (8)$$

and extend the radius to which we measure the stellar mass, bringing the two values into agreement, within errors ($\log[M_{\text{Chabrier, Spitzer}}/M_\odot] = 9.9$ and 9.6 and $\log[M_{\text{VHS, total}}/M_\odot] = 9.7$ and 9.5, for NGC 7162 and NGC 7162A, respectively). We use VHS rather than *Spitzer* data to provide consistency in the derived stellar masses of the group spirals as there are no *Spitzer* observations of ESO 288-G025 and ESO 288-G033. Additionally, VHS covers nearly the entire Southern hemisphere and will be complementary to WALLABY for providing stellar maps.

5.3 Vertical Density

For both the gaseous and stellar disks, we must consider the vertical density profile, $\rho(z)$, although there is no consistent method used for their modelling (e.g. Westmeier et al. 2011, and references therein). The most commonly used vertical density profiles use either infinitely thin gas and/or stellar disks or a density distribution with a $\text{sech}^2(z/z_0)$ vertical dependence (based on studies of edge-on spiral galaxies by van der Kruit & Searle 1981a,b):

$$\rho(r, z) = \rho(r) \text{sech}^2(z/z_0), \quad (9)$$

where z_0 is the scale height of the disk. In this work, we model the gas as an infinitely thin disk and the stellar disk vertical density following equation 9 and assume a scale length-to-scale height ratio of $h/z_0 = 5$ (e.g. van der Kruit & Searle 1981a). We calculate the scale length, h , using stellar surface density profiles determined using $5''$ rings, which better constrains the radial variation in the stellar surface density with higher resolution in the inner region of the galaxy disks. NGC 7162 has scale length of $h = 6.57 \pm 0.05 \text{ kpc}$ and a scale height of $z_0 = 1.31 \pm 0.05 \text{ kpc}$. Likewise, NGC 7162A has a scale length of $h = 4.65 \pm 0.05 \text{ kpc}$

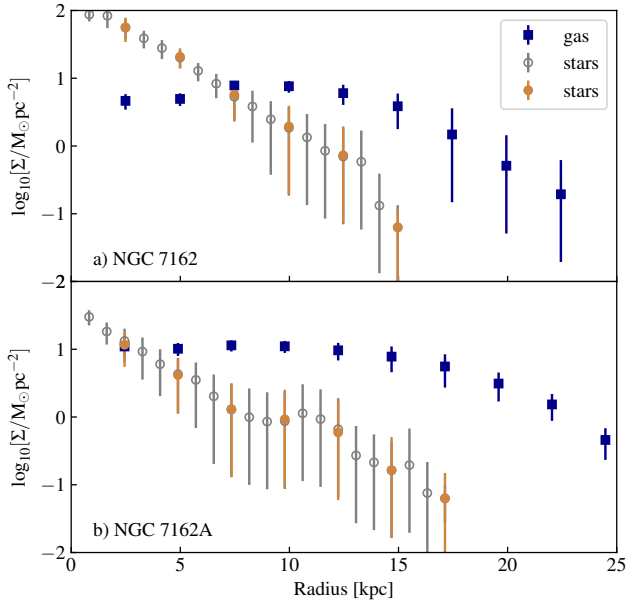


Figure 9. Stellar (filled, orange circles) and gaseous (filled, blue squares) surface densities for NGC 7162 (panel a) and NGC 7162A (panel b) using 15'' width rings. The stellar surface density determined using 5'' width rings is shown with empty, grey circles. The stellar surface densities are the average of the *J*- and *K*-band surface densities.

and a scale height of $z_0 = 0.93 \pm 0.05$ kpc. We obtain the same stellar surface density profile (average of *J*- and *K*-bands) for NGC 7162 and NGC 7162A using either 5'' and 15'' rings (Fig. 9, empty grey and filled orange circles, respectively). We also considered the case of the gas disk having the same scale height as the stellar disk. However, this has only a small affect of lowering the gas velocity by $\sim 1 \text{ km s}^{-1}$ at all radii and increasing the derived dark matter mass by ~ 0.1 dex.

5.4 Dark Matter Component

The third component to the mass model is the dark matter halo, which can be modelled following a number of different profiles. In this work, we only use a pseudo-isothermal profile as we are unable to differentiate among different dark matter profiles due to the low resolution of the central region of NGC 7162 and NGC 7162A. The pseudo-isothermal model (e.g. Begeman et al. 1991) is a physically motivated model with a constant central density with the density profile given by,

$$\rho(r) = \frac{\rho_0}{1 + (r/r_c)^2}, \quad (10)$$

where ρ_0 is the central density and r_c is the core radius. The pseudo-isothermal velocity profile is given by,

$$v^2(r) = 4\pi G \rho_0 r_c^2 \left[1 + \frac{r_c}{r} \arctan\left(\frac{r}{r_c}\right) \right]. \quad (11)$$

5.5 Modelling

We use the GISPY task ROTMAS for our mass modelling of NGC 7162 and NGC 7162A. The inputs into ROTMAS are

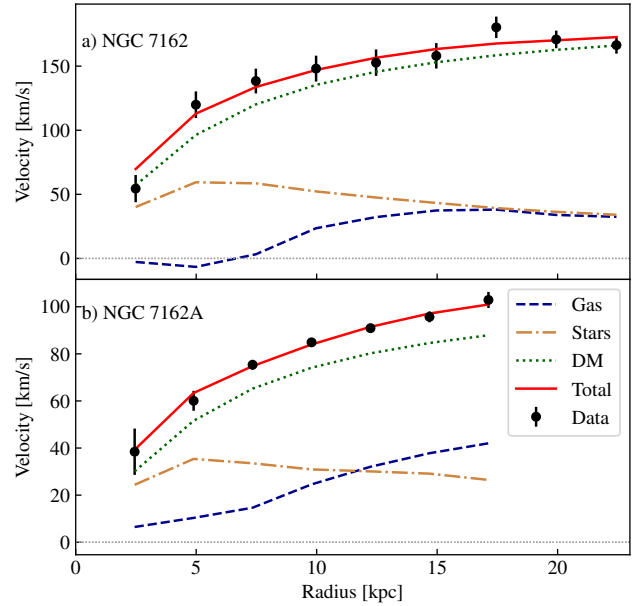


Figure 10. Rotation curve contributions for gas (dashed blue), stars (dot-dashed orange), dark matter (dotted green) and total (solid red) from mass modelling with ROTMAS for NGC 7162 (panel a) and NGC 7162A (panel b). Also plotted is the observed rotation curve (black points).

the observed rotation curve from the tilted ring fit to the entire galaxy, the gaseous and stellar surface densities, our selected vertical stellar density distribution given by equation 9, the stellar disk scale height and our chosen dark matter density profile (pseudo-isothermal). We do not include a bulge component in our modelled stellar surface density profile as, according to their morphological classifications (Table 3), the galaxies do not have prominent bulges. We fix the gaseous and stellar scaling factors, f_{gas} and f_* , to unity, leaving only the dark matter profile parameters, ρ_0 and r_c , free. We also tested leaving f_{gas} as a free parameter, however this did not significantly alter the derived dark matter masses. For NGC 7162 and NGC 7162A, we fit out to the same radius to which we calculated dynamical masses (20.3 and 15.5 kpc, respectively). We perform the mass modelling for a single dark matter profile with fixed gaseous and stellar scaling factors because of our limited resolution and inability to resolve the galaxies' central region (i.e. where we would be able to distinguish between different models).

In Fig. 10, we show our mass models for NGC 7162 (panel a) and NGC 7162A (panel b). We note the negative velocities of the gas at radii < 7.5 kpc in NGC 7162 do not mean the gas is counter-rotating to the rest of the disk, but is due to test particles in the modelling having a net outward force resulting in a negative v_{gas}^2 (Westmeier et al. 2011). This gives an imaginary velocity value, which is represented by negative velocities. Our derived dark matter masses are in agreement with our results from estimating dynamical masses and show both galaxies are dark matter dominated ($> 81\%$, Table 6).

Table 4. NGC 7162 tilted ring model fit parameters and their errors, and gaseous and stellar mass surface densities and their RMS deviations. Parameters: r - radius, i - inclination, θ - position angle, v_{rot} - rotational velocity, Σ_*^J - J -band stellar mass surface density, Σ_*^K - K -band stellar mass surface density, Σ_* - average stellar mass surface density, Σ_{gas} - gas mass surface density.

r [arcsec]	r [kpc]	i [degrees]	θ [degrees]	v_{rot} [km s ⁻¹]	Σ_*^J [M _⊙ pc ⁻²]	Σ_*^K [M _⊙ pc ⁻²]	Σ_* [M _⊙ pc ⁻²]	Σ_{gas} [M _⊙ pc ⁻²]
15	2.49	71 ± 4	20 ± 2	54 ± 11	47.4 ± 25.8	65.3 ± 36.8	56.4 ± 22.1	4.6 ± 1.2
30	4.99	72 ± 2	14 ± 1	120 ± 10	18.3 ± 8.0	23.2 ± 11.4	20.8 ± 6.9	5.0 ± 1.1
45	7.48	61 ± 2	13 ± 1	138 ± 10	5.5 ± 3.2	5.9 ± 6.0	5.7 ± 3.3	7.8 ± 1.0
60	9.98	58 ± 2	16 ± 1	148 ± 10	2.0 ± 1.8	1.9 ± 3.8	1.9 ± 2.0	7.6 ± 1.5
75	12.47	57 ± 2	16 ± 1	153 ± 10	0.8 ± 1.6	0.7 ± 1.9	0.7 ± 1.2	6.0 ± 2.0
90	14.96	55 ± 2	14 ± 1	158 ± 10	0.1 ± 0.1	0.1 ± 0.1	0.1 ± 0.1	3.9 ± 2.1
105	17.45	46 ± 5	17 ± 1	180 ± 8	—	—	—	1.5 ± 2.1
120	19.94	49 ± 3	17 ± 1	171 ± 7	—	—	—	0.5 ± 0.9
135	22.44	55 ± 4	21 ± 2	166 ± 7	—	—	—	0.2 ± 0.4

Table 5. NGC 7162A tilted ring model fit parameters and gaseous and stellar mass surface densities. Parameters the same as Table 4.

r [arcsec]	r [kpc]	i [degrees]	θ [degrees]	v_{rot} [km s ⁻¹]	Σ_*^J [M _⊙ pc ⁻²]	Σ_*^K [M _⊙ pc ⁻²]	Σ_* [M _⊙ pc ⁻²]	Σ_{gas} [M _⊙ pc ⁻²]
15	2.45	34 ± 11	18 ± 6	38 ± 10	9.7 ± 5.9	13.6 ± 11.5	11.7 ± 6.2	11.0 ± 2.3
30	4.89	44 ± 5	21 ± 2	60 ± 4	3.6 ± 2.4	4.7 ± 6.2	4.2 ± 3.1	10.2 ± 2.2
45	7.34	40 ± 2	19 ± 1	75 ± 2	1.2 ± 1.4	1.4 ± 3.7	1.3 ± 1.8	11.4 ± 2.2
60	9.79	38 ± 1	18 ± 1	85 ± 2	0.7 ± 1.2	1.1 ± 3.3	0.9 ± 1.6	11.1 ± 2.2
75	12.23	37 ± 1	18 ± 1	91 ± 2	0.6 ± 1.2	0.6 ± 2.0	0.6 ± 1.1	9.6 ± 2.8
90	14.68	36 ± 2	19 ± 1	96 ± 2	0.3 ± 0.7	0.1 ± 0.3	0.2 ± 0.3	7.8 ± 3.2
105	17.13	34 ± 3	19 ± 1	103 ± 3	0.1 ± 0.1	0.1 ± 0.1	0.1 ± 0.1	5.6 ± 2.9
120	19.59	26 ± 6	19 ± 1	130 ± 4	—	—	—	3.1 ± 1.4
135	22.03	18 ± 26	20 ± 4	182 ± 6	—	—	—	1.5 ± 0.7
150	24.48	11 ± 148	16 ± 16	319 ± 7	—	—	—	0.5 ± 0.2

Table 6. Mass modelling parameters using a pseudo-isothermal dark matter density profile for NGC 7162 and NGC 7162A. ρ_0 is the central density, r_c is the core radius, χ_{red}^2 is the reduced χ^2 goodness of fit, $\log(M_{\text{DM}}/M_{\odot})$ is the dark matter mass and f_{DM} is the dark matter fraction.

ISO Parameter	NGC 7162	NGC 7162A
r_c [kpc]	4.09 ± 0.70	4.35 ± 0.39
ρ_0 [M _⊙ pc ⁻³]	41.90 ± 10.95	11.80 ± 1.36
χ_{red}^2	0.91	0.41
$\log(M_{\text{DM}}/M_{\odot})$	11.1 ± 0.2	10.4 ± 0.2
f_{DM}	0.95	0.81

6 HI GAS MASS AND DEFICIENCY

Following Haynes & Giovanelli (1984) and Cortese et al. (2011), we determine if the group spirals are HI deficient, normal or rich compared to similar field spirals by calculating the expected galaxy HI mass as a function of galaxy morphology and size,

$$\log(M_{\text{HI,exp}}/M_{\odot}) = a_{\text{HI}} + b_{\text{HI}} \times \log\left(\frac{hD_{25}}{\text{kpc}}\right) - 2 \log(h), \quad (12)$$

where $h = H_0/100 \text{ km s}^{-1} \text{ Mpc}^{-1}$, D_{25} is the optical 25 mag arcsec⁻² B -band diameter and a_{HI} and b_{HI} are morphological type dependent coefficients (see table 3 from Boselli & Gavazzi 2009). The HI deficiency is then defined to be,

$$\text{DEF}_{\text{HI}} = \log(M_{\text{HI,exp}}/M_{\odot}) - \log(M_{\text{HI,obs}}/M_{\odot}). \quad (13)$$

We obtain morphology classifications and calculate galaxy diameters from NED (Table 3). We used the HI masses from ATCA for NGC 7162 and NGC 7162A for calculating their deficiencies as our ATCA spectra agree with HIPASS and recover more of the flux than ASKAP-12, hence we are less likely to underestimate DEF_{HI} . We calculate the HI deficiencies for ESO 288-G025 and ESO 288-G033 using the HI masses from ASKAP, as these galaxies do not have the same issues.

NGC 7162, NGC 7162A and ESO 288-G033 have HI excesses of 0.72, 0.95 and 0.66 dex, respectively. The excesses in these galaxies indicate that they have either accreted additional gas or are yet to be affected by the group environment, which would generally cause galaxies near the group centre to lose gas and become HI deficient. ESO 288-G025 has a much lower excess of 0.33 dex. Kilborn et al. (2009) and Rasmussen et al. (2012) only consider galaxies to have a HI deficiency if $|\text{DEF}_{\text{HI}}| > 0.30$ and > 0.45 , respectively, to account for uncertainties in diameters, HI masses and galaxy morphologies causing the apparent deficiencies. Here we take a conservative value of only considering galaxies with $|\text{DEF}_{\text{HI}}| > 0.45$ having a HI deficiency or excess. Hence, we do not consider ESO 288-G025 to have a HI excess.

7 DISCUSSION

In this work, we search for signs of interactions within the NGC 7162 group, primarily between NGC 7162 and

NGC 7162A. However, we do not identify any morphological signs of interactions or extended H I emission around NGC 7162 or NGC 7162A at ASKAP-12 resolution and sensitivity. We could expect to find evidence of interactions as the largest and approximately central galaxy of this group, NGC 7166, is an early type elliptical galaxy, suggesting that one or more merger events likely occurred in the group's history. It is possible that the merger occurred sufficiently long in the past that most signs have disappeared as there is no H I detected around NGC 7166 and all detected gas is confined to the six detected galaxies. We can place an upper limit on the column density of any extra-planar gas of $< 9.5 \times 10^{18} \text{ cm}^{-2}$ per 4 km s^{-1} channel for emission filling the $39'' \times 34''$ beam using our $5 \sigma \sim 11.5 \text{ mJy beam}^{-1}$ threshold. However, we can look for internal indications of interactions within the galaxies in H I.

- (i) We start with the most promising candidate, NGC 7162A, which appears to have a small twist in position angle between velocity field contours at the galaxy's centre compared with the outer regions (Fig. 2 row b, centre column). We also see this in the derived position angle from the tilted ring fitting to the full disk. However there is large uncertainty when looking at either the approaching or receding sides separately and the position angle is approximately constant across all radii within the errors (Fig. 7e). The position angles from the $25 \text{ mag arcsec}^{-2}$ *B*-band image and the value derived from the H I gas kinematics from SoFiA are offset by $\sim 40^\circ$, indicating the gas does not rotate in accordance with the galaxy's optical major axis. This, along with the possible small twist in the position angle with radius, could indicate that an interaction occurred in the group's past, either sufficiently long ago that there are no other obvious signs of the interaction or that we simply are unable to detect any morphological signs due to the imaging limitations of our observations.

In this group, NGC 7162A is the most H I rich galaxy with a H I mass excess of ~ 0.95 dex compared with isolated galaxies. This excess is surprising due to the presence of neighbouring galaxies with projected distances of ~ 126 kpc (NGC 7162 and NGC 7166), placing NGC 7162A in the densest part of the group, where galaxies are more commonly H I deficient. The excess gas is unlikely to have been removed from NGC 7162, which is also H I rich. However we are unable to identify an origin of the excess gas as we cannot detect any faint extra-planar gas inflowing onto NGC 7162A from either the ASKAP-12 or ATCA data (Fig. 2 left column, row b). Although NGC 7162A is H I rich, it is normal with regards to its H I to stellar mass ratio, $\log(M_{\text{HI}}/M_*)$, and specific star formation rate, $\log(\text{sSFR})$, as it follows the scaling relations in figure 5 from Catinella et al. (2018) for $\log(M_{\text{HI}}/M_*)$ vs $\log(M_*/M_\odot)$ and $\log(\text{sSFR})$ (Table 3). The gas fraction of NGC 7162A also agrees with the findings of Janowiecki et al. (2017) where group centrals have higher $\log(M_{\text{HI}}/M_*)$ at fixed $\log(M_*/M_\odot)$. NGC 7162A has a slightly lower star formation efficiency ($\text{SFE} = \text{SFR}/M_{\text{HI}}$) of $\log(\text{SFE}/\text{yr}) = -10.2$ compared with previous samples (e.g. $\log(\text{SFE}/\text{yr}) = -9.5, -9.95, -9.65$, Schiminovich et al. 2010; Huang et al. 2012; Wong et al. 2016, respectively), which could be due to it having a higher disk stability against star formation.

While we do not observe H I asymmetries in NGC 7162A

in either ASKAP or ATCA column density maps (Fig. 2 row 2, left column), it does appear asymmetric in *Spitzer* IRAC images and has asymmetry parameter values of 0.42 and 0.54 at $3.6 \mu\text{m}$ and $4.5 \mu\text{m}$, respectively (Holwerda et al. 2014). The asymmetry parameter is a quantitative measure of the asymmetry of a galaxy's brightness distribution with larger values indicating higher level of asymmetry. However, NGC 7162A is a Type 2 extended ultraviolet disk (XUV-disk) galaxy and appears clumpy, but symmetric in *GALEX* far-ultraviolet (FUV) images, demonstrating the need for multiple wavelengths to build up a more complete picture of the galaxy. Our classification of NGC 7162A as a Type 2 XUV-disk explains the lack of any identifiable near-infrared features in the outer disk by Laine et al. (2014). We can see this in Fig. 11c and d, where *GALEX* FUV emission extends to significantly larger radii compared with the VHS *K*-band emission concentrated in the galaxy's centre (for details on XUV-disk galaxies, see e.g. Thilker et al. 2007). The star forming disk of XUV-disk galaxies is much more extended than the older stellar population and questions remain on how these galaxies form (e.g. do tidal interactions provide the gas reservoir with a large distribution across the galaxy's disk?). WALLABY will resolve the H I in XUV-disk galaxies across the southern sky in a variety of environments and will be able to shed light on the relation between XUV-disk and H I gas morphology.

- (ii) NGC 7162 is H I rich by ~ 0.72 dex. Similarly to NGC 7162A, NGC 7162 follows the scaling relations in figure 5 from Catinella et al. (2018) for $\log(M_{\text{HI}}/M_*)$ vs $\log(M_*)$ and $\log(\text{sSFR})$ (Table 3). We find the inclination angle decreases towards the outer edge of the disk, starting at $\sim 70^\circ$ and decreasing to $\sim 55^\circ$ at the largest measured radius. Unlike NGC 7162A, NGC 7162 has good agreement between the position angles from the $25 \text{ mag arcsec}^{-2}$ *B*-band image with the derived value from the H I gas kinematics from SoFiA (10° vs 14° , respectively). Although NGC 7162 has high asymmetry parameter values of 0.74 and 0.51 from *Spitzer* IRAC $3.6 \mu\text{m}$ and $4.5 \mu\text{m}$ images, respectively (Holwerda et al. 2014), in *GALEX* FUV images it also appears symmetrical. NGC 7162 may also be an Type 2 XUV-disk galaxy, however its inclination is too high to say with certainty.

Referring to the ATCA column density map, we see that NGC 7162 does have a small amount of extended H I emission to the north east, pointing in the direction of NGC 7162A (Fig. 2 row 1, left column, thick grey contour). This shows that NGC 7162 has true extended emission, which we do not detect in the ASKAP-12 data because it is hidden in the residual sidelobes. The location of the extended emission and the lack of any extended emission detected around NGC 7162A suggests that this could be either very early stages of an interaction within the group or the end of the gas accretion onto NGC 7162 given its large H I excess. The extended emission is fairly faint and only accounts for $\sim 2\%$ of the galaxy's total H I mass.

- (iii) ESO 288-G025 has a H I excess of ~ 0.39 dex, which we consider to be H I normal (see Section 6). This is expected as ESO 288-G025 has the largest separation from the group (e.g. projected distance of ~ 305 kpc to NGC 7162). There is excellent agreement between the position angles from the optical *B*-band image with the derived value from the H I gas kinematics from SoFiA (53° vs 52° , respectively).

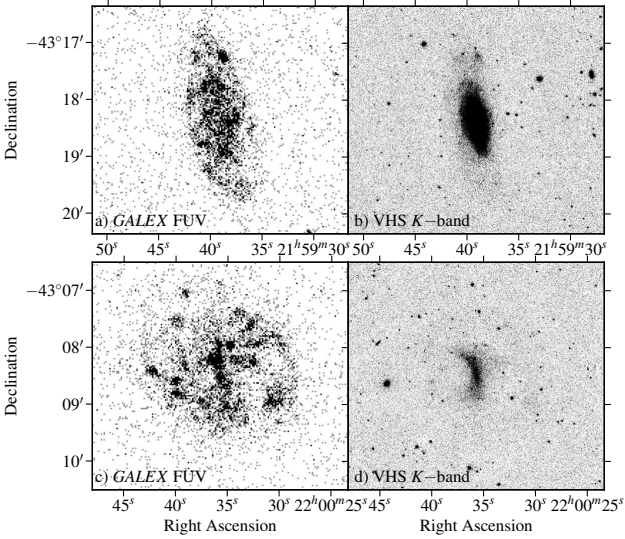


Figure 11. *GALEX* FUV and VHS *K*-band images of NGC 7162 (panels a and b) and NGC 7162A (panels c and d) illustrating that both galaxies appear much more symmetric in the UV than the IR. We also show that NGC 7162A is a Type 2 XUV galaxy with the emission from the FUV disk extending to much larger radii than the emission in the *K*-band.

- (iv) ESO 288-G033 is also H I rich (excess ~ 0.66 dex). There is a small offset (10°) between the position angles from the optical *B*-band image with the derived value from the H I gas kinematics from SoFiA. The ATCA column density map of ESO 288-G033 appears asymmetric with the H I emission more extended to the north (Fig. 2 row 4, left column, thick grey contour). However, this may be a result of the increased noise around ESO 288-G033, as it lies near the edge of the ATCA beam and we do not draw any conclusions on whether this indicates ESO 288-G033 is interacting.
- (v) We are unable to comment on internal signs of interactions in the dwarfs AM 2159-434 and J220338-431131 due to their small size, low signal-to-noise and lack of ancillary data for comparison.

The NGC 7162 group has a single X-ray luminosity upper limit for NGC 7166 of $\log(L_X) < 40.65$ ergs $^{-1}$ (Beuing et al. 1999) and is not defined as X-ray luminous. Previous studies of X-ray luminosity and H I deficiency found X-ray luminous groups tend to be more H I deficient relative to groups without X-ray emission (Chamaraux & Masnou 2004; Sengupta & Balasubramanyam 2006; Kilborn et al. 2009). Hence, the lack of X-ray emission from the NGC 7162 group is expected given the H I richness of the group, as all group spirals have H I excesses, with no galaxies detected to be deficient in H I.

All four spiral galaxies for which we can calculate dynamical or dark matter masses are dark matter dominated with dark matter fractions ranging from $f_{DM} = 0.81 - 0.95$. Although we are unable to use envelope tracing or tilted ring modelling for either dwarf galaxy, we attempt to derive approximate dynamical mass estimates up to a factor of $\sin^2(i)$, leaving the galaxy inclination angle as a free parameter. For AM 2159-434, we derive a dynamical mass estimate of $\log(M_{dyn} \times \sin^2(i)/M_\odot) \sim 9.1 \pm 0.4$ (where we as-

sume the rotational velocity to be half the velocity width, w_{50} , of the integrated spectrum, ~ 27 km s $^{-1}$, and the radius to be the radius in the moment 0 map, ~ 8.4 kpc). Similarly we derive an approximate dynamical mass estimate for J220338-431131 of $\log(M_{dyn} \times \sin^2(i)/M_\odot) \sim 8.9 \pm 0.4$ (assumed rotational velocity ~ 18 km s $^{-1}$ and radius ~ 10.9 kpc). As we mentioned, we are limited in our mass modelling to estimating the total dark matter content rather than differentiating among different dark matter density profiles. However, we still demonstrate the potential of ASKAP and WALLABY to provide dynamical and dark matter mass estimates for all HIPASS detected galaxies resolved by the ASKAP synthesised beam and map the dark matter distribution in gas-rich galaxies in the local Universe over the entire southern sky.

8 SUMMARY

In this work we have presented first results from WALLABY early science observations of the NGC 7162 galaxy group taken with ASKAP. We detected six galaxies in H I: NGC 7162, NGC 7162A, ESO 288-G025, ESO 288-G033, AM 2159-434 and J220338-431131. ESO 288-G033, AM 2159-434 and J220338-431131 are newly detected group members. Additionally, these are the first H I detections and distance measurements of the dwarf galaxies AM 2159-434 and J220338-431131.

Using archival HIPASS and ATCA observations, we performed validation checks on the ASKAP-12 observations. Minor calibration errors and the incomplete uv-coverage of ASKAP-12 result in residual sidelobes in the final image cube. This leads to a loss of flux in the brightest sources in the ASKAP observations compared with the archival ATCA and HIPASS data. Full ASKAP (36 antennas) will not be subject to these challenges. In the ASKAP-12 data we are unable to detect any morphological signs of interactions, although we do see extended H I emission to the north from NGC 7162 in the archival ATCA image cube. We are unable to see this H I extension in the ASKAP-12 image cube as it is either lost in the sidelobes present in the final data cube or resolved out by ASKAP. ASKAP also resolves out $\sim 40\%$ of the diffuse H I emission in NGC 7162A compared with HIPASS. Due to the H I richness of the spiral galaxies and the lack of significant indications of group interactions, it is likely that these galaxies are infalling for the first time and are yet to undergo any significant tidal interactions.

These ASKAP images have provided improved spatial and spectral resolution compared with HIPASS and ATCA observations and significantly increased field of view. The improved resolution and more circular beam compared with ATCA allow us to derive rotation curves and hence dynamical masses for all four spiral galaxies, and dark matter masses for NGC 7162 and NGC 7162A. We also attempt to derive rough estimates for the dynamical masses for the two dwarf galaxies. All observed spiral galaxies are dark matter dominated, with dark matter fractions $\sim 0.81 - 0.95$. However, we did not have sufficient resolution of the central region of the galaxies to test different dark matter models.

This work demonstrates the power of full WALLABY to estimate the dark matter content of gas-rich galaxies across the southern sky. The large field of view of ASKAP made it possible to observe the entire NGC 7162 group in a single

observation, while the centre of the observed 30 square degree field was focused on a different target, the NGC 7232 triplet (separated by $\sim 3.8^\circ$). Although the ASKAP-12 observations were carried out in ~ 175 h over 16 nights, full WALLABY will be able to achieve better sensitivity in a single 12 h observation, using 36 antennas, and study resolved galaxy groups at different stages of evolution across the entire southern sky. The mosaicked image cube produced with ASKAPSOFT is publicly available and can be downloaded at <https://doi.org/10.100.100/74066>.

ACKNOWLEDGEMENTS

This research was conducted by the Australian Research Council Centre of Excellence for All Sky Astrophysics in 3 Dimensions (ASTRO 3D), through project number CE170100013. This research has made use of the NASA/IPAC Extragalactic Database (NED) which is operated by the Jet Propulsion Laboratory, California Institute of Technology, under contract with the National Aeronautics and Space Administration. The Australia Telescope Compact Array and Parkes radio telescope are part of the Australia Telescope National Facility which is funded by the Australian Government for operation as a National Facility managed by CSIRO. This paper includes archived data obtained through the Australia Telescope Online Archive (<http://atoa.atnf.csiro.au>). The Australian SKA Pathfinder is part of the Australia Telescope National Facility which is managed by CSIRO. Operation of ASKAP is funded by the Australian Government with support from the National Collaborative Research Infrastructure Strategy. ASKAP uses the resources of the Pawsey Supercomputing Centre. Establishment of ASKAP, the Murchison Radioastronomy Observatory (MRO) and the Pawsey Supercomputing Centre are initiatives of the Australian Government, with support from the Government of Western Australia and the Science and Industry Endowment Fund. We acknowledge the Wajarri Yamatji as the traditional owners of the Observatory site. We also thank the MRO site staff.

This work is based in part on observations made with the Galaxy Evolution Explorer (GALEX). GALEX is a NASA Small Explorer, whose mission was developed in cooperation with the Centre National d'Etudes Spatiales (CNES) of France and the Korean Ministry of Science and Technology. GALEX is operated for NASA by the California Institute of Technology under NASA contract NAS5-98034.

This project used public archival data from the Dark Energy Survey (DES). Funding for the DES Projects has been provided by the U.S. Department of Energy, the U.S. National Science Foundation, the Ministry of Science and Education of Spain, the Science and Technology Facilities Council of the United Kingdom, the Higher Education Funding Council for England, the National Center for Supercomputing Applications at the University of Illinois at Urbana-Champaign, the Kavli Institute of Cosmological Physics at the University of Chicago, the Center for Cosmology and Astro-Particle Physics at the Ohio State University, the Mitchell Institute for Fundamental Physics and Astronomy at Texas A&M University, Financiadora de Estudos e Projetos, Fundação Carlos Chagas Filho de Amparo à Pesquisa do Estado do Rio de Janeiro, Conselho Nacional de Desen-

volvimento Científico e Tecnológico and the Ministério da Ciência, Tecnologia e Inovação, the Deutsche Forschungsgemeinschaft, and the Collaborating Institutions in the Dark Energy Survey.

The Collaborating Institutions are Argonne National Laboratory, the University of California at Santa Cruz, the University of Cambridge, Centro de Investigaciones Energéticas, Medioambientales y Tecnológicas-Madrid, the University of Chicago, University College London, the DES-Brazil Consortium, the University of Edinburgh, the Eidgenössische Technische Hochschule (ETH) Zürich, Fermi National Accelerator Laboratory, the University of Illinois at Urbana-Champaign, the Institut de Ciències de l'Espai (IEEC/CSIC), the Institut de Física d'Altes Energies, Lawrence Berkeley National Laboratory, the Ludwig-Maximilians Universität München and the associated Excellence Cluster Universe, the University of Michigan, the National Optical Astronomy Observatory, the University of Nottingham, The Ohio State University, the OzDES Membership Consortium, the University of Pennsylvania, the University of Portsmouth, SLAC National Accelerator Laboratory, Stanford University, the University of Sussex, and Texas A&M University.

Based in part on observations at Cerro Tololo Inter-American Observatory, National Optical Astronomy Observatory, which is operated by the Association of Universities for Research in Astronomy (AURA) under a cooperative agreement with the National Science Foundation.

REFERENCES

- Abbott T. M. C., et al., 2018, preprint, ([arXiv:1801.03181](https://arxiv.org/abs/1801.03181))
 Applebaum S. P., 1976, *IEEE Transactions on Antennas and Propagation*, **24**, 585
 Barnes D. G., et al., 2001, *MNRAS*, **322**, 486
 Begeman K. G., Broeils A. H., Sanders R. H., 1991, *MNRAS*, **249**, 523
 Beuing J., Dobereiner S., Bohringer H., Bender R., 1999, *MNRAS*, **302**, 209
 Boselli A., Gavazzi G., 2009, *aap*, **508**, 201
 Brough S., Forbes D. A., Kilborn V. A., Couch W., 2006, *Monthly Notices of the Royal Astronomical Society*, **370**, 1223
 Catinella B., et al., 2018, *MNRAS*, **476**, 875
 Chabrier G., 2003, *PASP*, **115**, 763
 Chamaraux P., Masnou J.-L., 2004, *MNRAS*, **347**, 541
 Chippendale A. P., et al., 2015, in 2015 International Conference on Electromagnetics in Advanced Applications (ICEAA), p. 541-544. pp 541-544 ([arXiv:1509.00544](https://arxiv.org/abs/1509.00544)), [doi:10.1109/ICEAA.2015.7297174](https://doi.org/10.1109/ICEAA.2015.7297174)
 Chung A., van Gorkom J. H., Kenney J. D. P., Crowl H., Vollmer B., 2009, *AJ*, **138**, 1741
 Cluver M. E., Jarrett T. H., Dale D. A., Smith J.-D. T., August T., Brown M. J. I., 2017, *ApJ*, **850**, 68
 Cornwell T. J., 2008, *IEEE Journal of Selected Topics in Signal Processing*, **2**, 793
 Cornwell T. J., Golap K., Bhatnagar S., 2008, *IEEE Journal of Selected Topics in Signal Processing*, **2**, 647
 Cortese L., Catinella B., Boissier S., Boselli A., Heinis S., 2011, *MNRAS*, **415**, 1797
 DeBoer D. R., et al., 2009, *IEEE Proceedings*, **97**, 1507
 Dénes H., Kilborn V. A., Koribalski B. S., 2014, *MNRAS*, **444**, 667
 Dressler A., 1980, *ApJ*, **236**, 351
 Driver S. P., et al., 2011, *MNRAS*, **413**, 971

- Duffy A. R., Meyer M. J., Staveley-Smith L., Bernyk M., Croton D. J., Koribalski B. S., Gerstmann D., Westerlund S., 2012, *MNRAS*, **426**, 3385
- English J., Koribalski B., Bland-Hawthorn J., Freeman K. C., McCain C. F., 2010, *AJ*, **139**, 102
- Fouque P., Gourgoulhon E., Chamaraux P., Paturel G., 1992, *A&AS*, **93**, 211
- Freeland E., Stilp A., Wilcots E., 2009, *AJ*, **138**, 295
- Giovanelli R., Haynes M. P., 1985, *ApJ*, **292**, 404
- Gourgoulhon E., Chamaraux P., Fouque P., 1992, *A&A*, **255**, 69
- Gunn J. E., Gott III J. R., 1972, *ApJ*, **176**, 1
- Hampson G., et al., 2012, in *Electromagnetics in Advanced Applications (ICEAA)*, 2012 International Conference on. pp 807–809, doi:10.1109/ICEAA.2012.6328742
- Hay S., O’Sullivan J., 2008, *Radio Science*, **43**
- Haynes M. P., Giovanelli R., 1984, *The Astronomical Journal*, **89**
- Haynes M. P., et al., 2018, preprint, (arXiv:1805.11499)
- Heald G., et al., 2011, *A&A*, **526**, A118
- Hess K. M., Wilcots E. M., 2013, *Astronomical Journal*, **146**
- Hess K. M., Cluver M. E., Yahya S., Leisman L., Serra P., Lucero D. M., Passmoor S. S., Carignan C., 2017, *Monthly Notices of the Royal Astronomical Society*, **464**, 957
- Heywood I., et al., 2016, *MNRAS*, **457**, 4160
- Holwerda B. W., et al., 2014, *ApJ*, **781**, 12
- Hotan A. W., et al., 2014, *Publ. Astron. Soc. Australia*, **31**, e041
- Huang S., Haynes M. P., Giovanelli R., Brinchmann J., 2012, *ApJ*, **756**, 113
- Jaffé Y. L., Smith R., Candlish G. N., Poggianti B. M., Sheen Y. K., Verheijen M. A., 2015, *MNRAS*, **448**
- Janowiecki S., Catinella B., Cortese L., Saintonge A., Brown T., Wang J., 2017, *MNRAS*, **466**, 4795
- Jones M. G., Haynes M. P., Giovanelli R., Moonman C., 2018, *MNRAS*, **477**, 2
- Kenney J. D. P., van Gorkom J. H., Vollmer B., 2004, *Aj*, **127**, 3361
- Kern K. M., Kilborn V. A., Forbes D. A., Koribalski B., 2008, *MNRAS*, **384**, 305
- Kilborn V. A., Koribalski B. S., Forbes D. A., Barnes D. G., Musgrave R. C., 2005, *Monthly Notices of the Royal Astronomical Society*, **356**, 77
- Kilborn V. A., Forbes D. A., Barnes D. G., Koribalski B. S., Brough S., Kern K., 2009, *Monthly Notices of the Royal Astronomical Society*, **400**, 1962
- Koribalski B. S., 2012, *Publ. Astron. Soc. Australia*, **29**, 359
- Koribalski B., Dickey J., 2004, *Monthly Notices of the Royal Astronomical Society*, **348**, 1255
- Koribalski B. S., López-Sánchez Á. R., 2009, *MNRAS*, **400**, 1749
- Koribalski B., Manthey E., 2005, *Monthly Notices of the Royal Astronomical Society*, **358**, 202
- Koribalski B. S., et al., 2018, *MNRAS*,
- Laine S., et al., 2014, *MNRAS*, **444**, 3015
- Larson R. B., Tinsley B. M., Caldwell C. N., 1980, *ApJ*, **237**, 692
- Lauberts A., Valentijn E. A., 1989, *The surface photometry catalogue of the ESO-Uppsala galaxies*
- Longhetti M., Saracco P., 2009, *MNRAS*, **394**, 774
- Maia M. A. G., da Costa L. N., Latham D. W., 1989, *ApJS*, **69**, 809
- McConnell D., et al., 2016, *Publ. Astron. Soc. Australia*, **33**, e042
- McMahon R. G., Banerji M., Gonzalez E., Koposov S. E., Bejar V. J., Lodieu N., Rebolo R., VHS Collaboration 2013, *The Messenger*, **154**, 35
- Meyer M. J., et al., 2004, *MNRAS*, **350**, 1195
- Moore B., Katz N., Lake G., Dressler A., Oemler A., 1996, *Nature*, **379**, 613
- Moore B., Lake G., Katz N., 1998, *ApJ*, **495**, 139
- Moore B., Lake G., Quinn T., Stadel J., 1999, *MNRAS*, **304**, 465
- Muñoz-Mateos J. C., et al., 2015, *ApJS*, **219**, 3
- Navarro J. F., Frenk C. S., White S. D. M., 1997, *ApJ*, **490**, 493
- Odekon M. C., et al., 2016, *The Astrophysical Journal*, **824**, 1
- Oh S.-H., de Blok W. J. G., Walter F., Brinks E., Kennicutt Jr. R. C., 2008, *AJ*, **136**, 2761
- Oh S.-H., de Blok W. J. G., Brinks E., Walter F., Kennicutt Jr. R. C., 2011, *AJ*, **141**, 193
- Oh S.-H., et al., 2015, *AJ*, **149**, 180
- Oh S.-H., Staveley-Smith L., Spekkens K., Kamphuis P., Koribalski B. S., 2018, *MNRAS*, **473**, 3256
- Oosterloo T. A., Morganti R., Sadler E. M., van der Hulst T., Serra P., 2007, *A&A*, **465**, 787
- Pisano D. J., Barnes D. G., Staveley-Smith L., Gibson B. K., Kilborn V. A., Freeman K. C., 2011, *Astrophysical Journal, Supplement Series*, **197**
- Planck Collaboration et al., 2016, *A&A*, **594**, A13
- Rasmussen J., Ponman T. J., Mulchaey J. S., 2006, *MNRAS*, **370**, 453
- Rasmussen J., et al., 2012, *ApJ*, **747**, 31
- Rau U., Cornwell T. J., 2011, *A&A*, **532**, A71
- Reeves S. N., Sadler E. M., Allison J. R., Koribalski B. S., Curran S. J., Pracy M. B., 2015, *MNRAS*, **450**, 926
- Rogstad D. H., Lockhart I. A., Wright M. C. H., 1974, *ApJ*, **193**, 309
- Salpeter E. E., 1955, *ApJ*, **121**, 161
- Sancisi R., Allen R. J., 1979, *A&A*, **74**, 73
- Sault R. J., Teuben P. J., Wright M. C. H., 1995, in Shaw R. A., Payne H. E., Hayes J. J. E., eds, *Astronomical Society of the Pacific Conference Series Vol. 77, Astronomical Data Analysis Software and Systems IV*. p. 433 (arXiv:astro-ph/0612759)
- Schiminovich D., et al., 2010, *MNRAS*, **408**, 919
- Schinkel A. E. T., Bock D. C.-J., 2016, in *Ground-based and Airborne Telescopes VI*. p. 99062A, doi:10.1117/12.2233920
- Sengupta C., Balasubramanyam R., 2006, *MNRAS*, **369**, 360
- Serra P., et al., 2013, *Monthly Notices of the Royal Astronomical Society*, **428**, 370
- Serra P., et al., 2015a, *MNRAS*, **448**, 1922
- Serra P., et al., 2015b, *MNRAS*, **452**, 2680
- Sofue Y., Rubin V., 2001, *ARA&A*, **39**, 137
- Solanes J. M., Manrique A., García-Gómez C., González-Casado G., Giovanelli R., Haynes M. P., 2001, *ApJ*, **548**, 97
- Springob C. M., et al., 2014, *MNRAS*, **445**, 2677
- Taylor E. N., et al., 2011, *MNRAS*, **418**, 1587
- Thilker D. A., et al., 2007, *ApJS*, **173**, 538
- Tully R. B., 1987, *ApJ*, **321**, 280
- Vogelaar M. G. R., Terlouw J. P., 2001, in Harnden Jr. F. R., Primini F. A., Payne H. E., eds, *Astronomical Society of the Pacific Conference Series Vol. 238, Astronomical Data Analysis Software and Systems X*. p. 358
- Westmeier T., Braun R., Koribalski B. S., 2011, *MNRAS*, **410**, 2217
- Westmeier T., Koribalski B. S., Braun R., 2013, *MNRAS*, **434**, 3511
- Wevers B. M. H. R., Appleton P. N., Davies R. D., Hart L., 1984, *a&a*, **140**, 125
- Wilson W. E., et al., 2011, *MNRAS*, **416**, 832
- Wong O. I., Meurer G. R., Zheng Z., Heckman T. M., Thilker D. A., Zwaan M. A., 2016, *MNRAS*, **460**, 1106
- Wright A. H., et al., 2016, *MNRAS*, **460**, 765
- Zabludoff A. I., Mulchaey J. S., 1998, *ApJ*, **496**, 39
- Zwaan M. A., Meyer M. J., Staveley-Smith L., Webster R. L., 2005, *MNRAS*, **359**, L30
- de Blok W. J. G., McGaugh S. S., Rubin V. C., 2001, *AJ*, **122**, 2396
- de Blok W. J. G., Walter F., Brinks E., Trachternach C., Oh S.-H., Kennicutt Jr. R. C., 2008, *AJ*, **136**, 2648
- de Blok W. J. G., et al., 2017, preprint, (arXiv:1709.08458)
- de Vaucouleurs G., de Vaucouleurs A., Corwin Jr. H. G., Buta R. J., Paturel G., Fouqué P., 1991, *Third Reference Catalogue of Bright Galaxies. Volume I: Explanations and references.*

Volume II: Data for galaxies between 0^h and 12^h . Volume III: Data for galaxies between 12^h and 24^h .

van der Hulst J. M., Terlouw J. P., Begeman K. G., Zwitter W., Roelfsema P. R., 1992, in Worrall D. M., Biemesderfer C., Barnes J., eds, *Astronomical Society of the Pacific Conference Series Vol. 25, Astronomical Data Analysis Software and Systems I*. p. 131

van der Kruit P. C., Searle L., 1981a, *A&A*, **95**, 105

van der Kruit P. C., Searle L., 1981b, *A&A*, **95**, 116

This paper has been typeset from a $\text{\TeX}/\text{\LaTeX}$ file prepared by the author.